High-Speed Granular Chute Flows

A. J. HOLYOAKE AND J. N. MCELWAINE†

Department of Applied Mathematics and Theoretical Physics, University of Cambridge, Wilberforce Road, Cambridge CB3 0WA, UK

(Received 14 June 2012; revised ?; accepted?.)

This paper reports experimental findings on the flow of sand down a steep chute. Nearly all granular flow models have a maximum value for the friction and therefore predict that flows on steep slopes will accelerate at a constant rate until the interaction with the ambient fluid becomes important. This prediction has not been tested by previous work, which has focused on relatively low slope angles where steady, fully developed flows occur after short distances. We test this by investigating flows over a much greater range of slope angles (30–50°) and flow depths (4–130 particle diameters). We examine flows with two basal conditions, one flat and frictional, the other bumpy. The latter imposes a no-slip condition for slow, deep flows, but permits some degree of slip for high flow velocities. The data suggests that friction can be much larger than theories such as the $\mu(I)$ rheology proposed in Jop *et al.* (2006) suggest and that there may be constant velocity states above the angle of vanishing h_{stop}. Though these flows do not vary in time, all but the flows on the bumpy base at low inclinations accelerate down the slope. A recirculation mechanism sustains flows with a maximum mass flux of $20\,\mathrm{kg\,s^{-1}}$, allowing observations to be made at multiple points for each flow for an indefinite period. Flows with Froude number in the range 0.1–25 and bulk inertial number 0.1–2.7 were observed in the dense regime, with surface velocities in the range 0.2–5.6 $\mathrm{m\,s^{-1}}$. Previous studies have focused on $I \lessapprox 0.5$. We show that a numerical implementation of the $\mu(I)$ rheology, does not fully capture the accelerating dynamics or the transverse velocity profile on the bumpy base. We also observe the transverse separation of the flow into a dense core flanked by dilute regions and the formation of longitudinal vortices.

1. Introduction

Dense granular flows occur frequently in both nature and industry, yet, despite their prevalence, they remain poorly understood. The lack of a generally applicable constitutive relation means that a theory encapsulating their dynamics for all situations remains illusive. Depending on the local conditions, granular materials can behave as a solid, liquid or gas. As the size of the grains and the length scales of the flow are of the same order of magnitude, there is a lack of separation of scales. This, along with the absence of thermodynamic equilibrium, means that a traditional continuum approximation approach such as the Navier-Stokes equation for Newtonian fluids, has limited utility when trying to capture the diverse range of behaviours.

At one extreme, for flows under slow and small deformation, soil mechanics can give good predictions (Jackson 1983). For very energetic, dilute flows, where the dynamics are dominated by uncorrelated, binary collisions, modified kinetic theory makes good quantitative predictions (Goldhirsch 2003; Jenkins & Richman 1985; Mitarai & Nakanishi 2005) and some theories attempt to include correlations (Jenkins & Berzi 2010). Between these two extremes lies a flowing regime where the volume fraction $\phi > 0.5$ and

† Email address for correspondence: jnm11@cam.ac.uk

friction, collisions and force chains each play an important role in the dynamics. While this regime has received a large amount of theoretical attention, the validity of models and observations is restricted to a small number of experiments, with little variation in the control parameters.

The simple geometry of the inclined chute not only provides a good basis for studying natural gravity flows such as debris flows and avalanches, but is directly relevant to industrial transport contexts. As a result it has formed the basis of many experimental studies e.g. Ahn *et al.* (1991, 1992); Patton *et al.* (1987); Louge & Keast (2001); Delannay *et al.* (2007) over a variety of surface conditions. These studies focus on fully developed flows where all quantities are constant in time and where there is no flow development down the slope. The behaviour of these flows is captured by the flow rule

$$\mathrm{Fr} = -\gamma + \beta \frac{h}{h_{\mathrm{stop}}(\theta)} \tag{1.1}$$

for material constants γ and β (Pouliquen 1999). We define the bulk Froude number as

$$\mathrm{Fr} = \frac{u_{\mathrm{s}}}{\sqrt{gh\cos\theta}}. \tag{1.2}$$

Where u_{s} is the average surface velocity, g the acceleration due to gravity and h the flow thickness. Alternative definitions of Fr exist in the literature where the depth and width averaged velocity $\bar{u}$ is used instead of u_{s}, however, only the surface velocity is known in our experiments so it is convenient to use this definition. The height $h_{\mathrm{stop}}(\theta)$ is the depth of the deposit left after a flow on a plane at an inclination θ has arrested and depends both on the material and the basal conditions. The minimum angle for which $h_{\mathrm{stop}} = 0$ is denoted by θ_2 and determining its value is equivalent to specifying the maximal frictional resistance of the material under shearing for flows obeying equation (1.1). For inclinations above θ_2 we have $h_{\mathrm{stop}} = 0$ and the $\mu(I)$ model predicts that the material accelerates indefinitely.

In order to track the development of accelerating flows on inclinations greater than θ_2, multiple measurements must be made along the chute. In our experimental set-up, the problem of maintaining a flow for a sufficiently long time to achieve this has been solved by using a recirculation system. After initiation, the flow rapidly becomes steady in time, but accelerates down the slope. Along with the Froude number, Fr, and the inclination θ, the flow is characterised by its non-dimensional height $n = h/d$, which measured the flow height in particle diameters and is controlled indirectly by changing the mass flux.

We investigate accelerating flows using two different bases: one bumpy, which usually imposes a no-slip boundary condition, and a flat, frictional base which permits slip. The two control parameters in the experiment are the mass flux, q, and the inclination of the chute, θ. Varying these determines the velocity and height of the flow down the chute. Height and velocity can then be used to calculate the total effective friction coefficient μ, which can then be compared to predictions using the $\mu(I)$ rheology of Jop *et al.* (2006) described below. The flows presented here are all contained by flat walls. Despite this, the transverse velocity profiles vary considerably between the different basal conditions, indicating a complex boundary interaction.

The $\mu(I)$ rheology which provides good agreement with a number of experiments at small inclinations (see MiDi 2004), equates the shear stress and the pressure using a phenomenological expression for the internal friction coefficient

$$\mu_i(I) = \frac{\mu_1 I_0 + \mu_2 I}{I_0 + I} \tag{1.3}$$

We have adopted the subscript i to distinguish the friction in a continuum model from the total friction μ which refers to dynamics of a slice of material averaged across the width and depth of the chute. In equation 1.3 μ_1 is the lower limit for the material's frictional resistance attained for vanishing I and $\mu_2 = \tan\theta_2$ is the maximum attained in the limit as $I \to \infty$. I_0 sets the scale over which μ_i changes and is usually taken to be constant and a function of the material properties. However, Jop *et al.* (2005) shows that it has a non-trivial, albeit weak dependence on the inclination of the flow over the range studied. The inertial number I, which is the square root of the Savage number (Savage (1984)), or the Coulomb number (Ancey *et al.* 1999), is defined as the ratio of the microscopic $d/\sqrt{P/\rho}$ and macroscopic $1/|\dot{\gamma}_{ij}|$ deformation timescales and is given by

$$I = \frac{|\dot{\gamma}_{ij}|\, d}{\sqrt{P/\rho}}, \tag{1.4}$$

where $|\dot{\gamma}_{ij}|$ is the absolute value of the local shear rate, d is the particle diameter, P is the particle pressure and ρ is the density of a single particle. Other slightly different definitions are sometimes used that incorporate the packing fraction. The value of the inertial number gives some indication of the nature of the flow: for high values of I, the flow is highly energised, dilute and in the collisional regime and for small I, the deformation is slow and quasi-static. We consider $I \approx 0.5$ as marking a transition to high-speed flows, but there is no discontinuous change in flow regime. The dense fluid regime investigated in this paper lies between these two extremes. We can use typical values for the local shear rate $|\dot{\gamma}_{ij}| = u_s/h$ and the basal pressure $P = \rho g h \cos\theta$ to define the bulk inertial parameter as

$$I_b = \frac{u_s d}{\sqrt{g h^3 \cos\theta}} = \frac{\mathrm{Fr}}{n}. \tag{1.5}$$

In our experiments I_b is in the range $0.1 < I_b < 2.7$ throughout which the flow remains in the dense regime. The upper limit of this range is much larger than in previous studies which have typically focused on the range $I_b < 0.5$ (MiDi 2004; Forterre & Pouliquen 2008).

In section 2 we set out the theoretical framework for describing these results. In section 3 we describe the experimental procedure and measurement techniques. Section 4 details our experimental findings. A numerical implementation of the $\mu(I)$ rheology is described in section 5, and the comparison with the experimental results is discussed in section 6.

2. Governing Equations

The depth integrated equations of motion, or Saint-Venant equations (Savage & Hutter 1989), provide a means of defining a macroscopic friction coefficient, or total friction, μ which measures the overall retardation of a slice of granular fluid due to the frictional forces exerted on the material by the boundaries. This stress is then transmitted through the material according to its rheology. We start by defining the mass flux, which is given by

$$q = \rho w \bar{\phi} \bar{u} h. \tag{2.1}$$

Here $\bar{u}$ is the mass averaged velocity at a position x down the slope, h is the flow height, which is assumed to be only a function of x, w is the chute width, ρ is the density of a particle and ϕ is the volume fraction. Previous studies (Louge & Keast 2001) have used non-invasive measurement techniques to show that ϕ is approximately

constant and this is in agreement with DEM simulations (Silbert *et al.* 2001), with the approximation improving for thicker flows. We can therefore assume incompressibility (that is $\phi = \text{const.}$) to write the depth-integrated conservation of mass as

$$\frac{\partial h}{\partial t} + \frac{\partial h\bar{u}}{\partial x} = 0. \tag{2.2}$$

For a steady flow we have $\partial_t = 0$, and therefore q is constant down the slope. Similarly, the x-component of the integrated conservation of momentum gives

$$\rho \frac{s_2}{s_1^2} \frac{\partial \left(h\bar{u}^2\right)}{\partial x} + \frac{\partial}{\partial x}\left(\frac{1}{2} g \cos\theta h^2\right) = gh\sin\theta - hF, \tag{2.3}$$

where the hydrostatic pressure $P = \rho g z \cos\theta$ is taken from the vertical (z) component and substituted into the horizontal component and the s_n are defined below. Here, we have assumed that the velocity is solely in the down-slope direction. We have chosen $z = 0$ to correspond to the free surface. We write the x-velocity, u, as the average surface velocity u_s multiplied by a function to give the full width y and depth z dependence:

$$u = u_\mathrm{s}\, f(y/w, z/h). \tag{2.4}$$

We define the s_n as the average value of f^n

$$s_n = \frac{1}{wh} \int\int f^n \,\mathrm{d}y\,\mathrm{d}z. \tag{2.5}$$

In this representation, f takes a value of 1 at a point on the surface. Since the flows are presumed to be symmetric and the walls exert resistive forces, we expect this to occur in the middle and therefore $f(1/2, 0) = 1$ with $f < 1$ at the walls. A flow with a no-slip basal condition gives $f(y/w, 1) = 0$, a flow with Bagnold depth dependence has $f \sim z^{3/2}$, and a plug flow has $f(y/w, z/h) = 1$. The first term on the right-hand side of equation (2.3) represents the gravitational forcing, while the second one, F, is the resistance of the material to flowing. The latter is dependent upon both the rheology and the interaction of the flow with the boundaries. We can eliminate derivatives of h in (2.3) using equation (2.2). Also using the relationship $\bar{u} = s_1 u_\mathrm{s}$, we obtain

$$\left(s_2 - \frac{1}{\mathrm{Fr}^2}\right) u_\mathrm{s} \frac{\mathrm{d}u_\mathrm{s}}{\mathrm{d}x} = g\sin\theta - F. \tag{2.6}$$

This demonstrates the change between subcritical and supercritical flow according to whether $\sqrt{s_2}\mathrm{Fr}$ is less than or greater than one. Using the divergence theorem, F can be written in terms of the stress tensor at the boundaries of the flow

$$hw\rho F = \int_0^h \int_0^w \frac{\partial \sigma_{xx}}{\partial x} \,\mathrm{d}y\,\mathrm{d}z + 2\int_0^h \sigma_{xy}|_{y=w} \,\mathrm{d}z + \int_0^w \sigma_{xz}|_{z=h} \,\mathrm{d}y. \tag{2.7}$$

The above expression assumes a symmetric flow about the centreline and no-stress condition at the free surface. The total friction, μ, is then defined as

$$\mu = \frac{F}{g\cos\theta}. \tag{2.8}$$

Assuming $f(y, z)$ is everywhere positive (that is no return flow) then $0 < s_n < 1$. For example, a plug flow has $s_1 = s_2 = 1$, while for linear shear we find $s_1 = \frac{1}{2}, s_2 = \frac{1}{3}$ and for a Bagnold profile $s_1 = \frac{3}{5}, s_2 = \frac{9}{20}$. In this derivation we have assumed that the lateral earth pressure coefficient is 1 (that is the horizontal and vertical normal stresses are equal) in accordance with the findings of Ertaş *et al.* (2001).

In steady, fully-developed flows, the acceleration is by definition 0, and $\mu = \tan\theta$. The factor $s_2 - \mathrm{Fr}^{-2}$ multiplying the advective acceleration in equation (2.6) gives some indication of the range of validity of the assumption of time-steady flow. For $\mathrm{Fr} > s_2^{-1/2}$, the downslope coordinate, x, behaves as a modified time coordinate and the flows are super-critical, with the upstream conditions left unaffected by downstream conditions. When $\mathrm{Fr} < s_2^{-1/2}$, the flow is sub-critical and the flow is determined by the down stream conditions. In both cases the existence of a time-steady state, and hence validity of equation (2.6) will depend on the boundary conditions.

3. Experimental Method

Our flows are generated by the equipment shown in figures 1 and 2. A crucial feature of the apparatus is the recirculation mechanism. The recirculation process starts with roughly 2000 kg of sand at rest in the collection hopper (A). This is fed to a screw conveyor (B) which when operating at its maximum capacity can move $22\,\mathrm{kg\,s^{-1}}$ of material to the bucket conveyor (C). This lifts the material 6 m vertically to the feed hopper (D). The feed hopper contains an overflow pipe (G) that ensures a constant head of sand is maintained. This is necessary to ensure a constant flow rate since our hopper is too small for the exit conditions to be governed by the Janssen effect (Janssen 1895). The exit of the hopper consists of a rectangular aperture of width 225 mm and of variable length which is controlled by a screw attached to a pulley. The angular position of the screw is given by a digital rotary encoder with one degree of rotation equivalent to 0.0139 mm of linear travel, giving very fine control over the aperture geometry. The aperture length can be anywhere from fully closed to 225 mm at its maximum. The sand falls freely from the aperture onto the chute (E) so that the conditions inside the chute do not affect the mass flow rate. The chute is mechanically isolated from the recirculation system so that vibrations do not affect the flow of the sand or the measurements. The inclination of the chute can be varied from 15° to 55° and is measured to an accuracy of 0.1° by a digital inclinometer. There were small variations in the inclination along the chute of around 0.1° due to it flexing under its own weight. The chute itself is 4 m by 0.25 m, of which the entire width and 3 m of length are observable experimentally. Whilst in the chute, measurements are made by instrumentation mounted on a hand operated traverse (F) located above. Finally, the sand falls freely from the chute onto the return chute (H) which deflects the sand back into the collection hopper. The machine is enclosed to contain dust and there is an extensive ventilation and filtering system which removes the finest particles from the material and the air in the laboratory.

3.1. *Material*

The material used in our experiments is a polydisperse bumpy quartz sand which, when new, has a size distribution shown in figure 3(a), with median diameter 1.24 mm and first and third quartiles at 1.03 mm and 1.48 mm respectively. The sand was sized using the Single Particle Optical Sizing technique detailed in White (2003) which typically gives a particle size 20–30% bigger than sieving for natural sands. The recirculation mechanism degrades the material and a considerable quantity of dust is produced initially. However, figure 3(b) shows that the distribution quickly tends to a steady state. New sand is periodically added to replace grains lost through the degradation process.

The limits of the frictional resistance in the $\mu(I)$ rheology can be ascertained by recording the value of the height h_{stop} over a range of θ. If the formation of a steady, non-accelerating layer of sand at a given inclination is possible, then the friction must exactly balance the gravitational force giving $\mu = \tan\theta$.

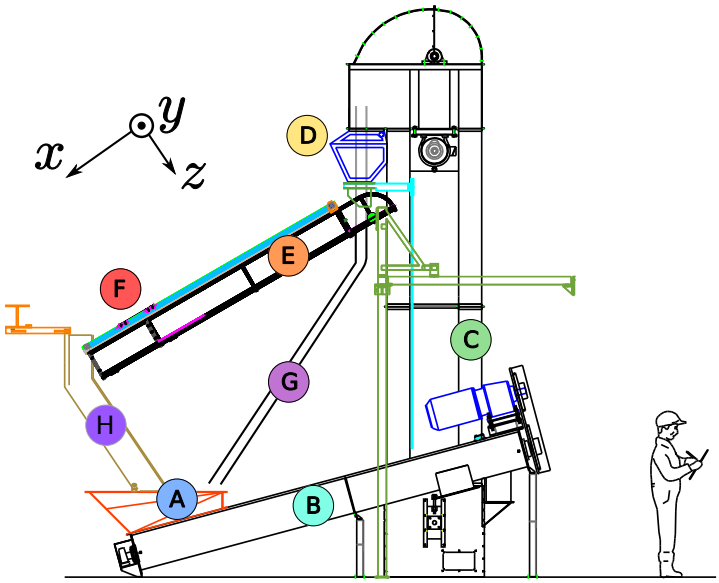

FIGURE 1. Diagram of Apparatus: (A) Collection Hopper (B) Screw Conveyor (C) Bucket Conveyor (D) Feed Hopper (E) Chute (F) Instrumentation and traverse (G) Overflow (H) Return Chute

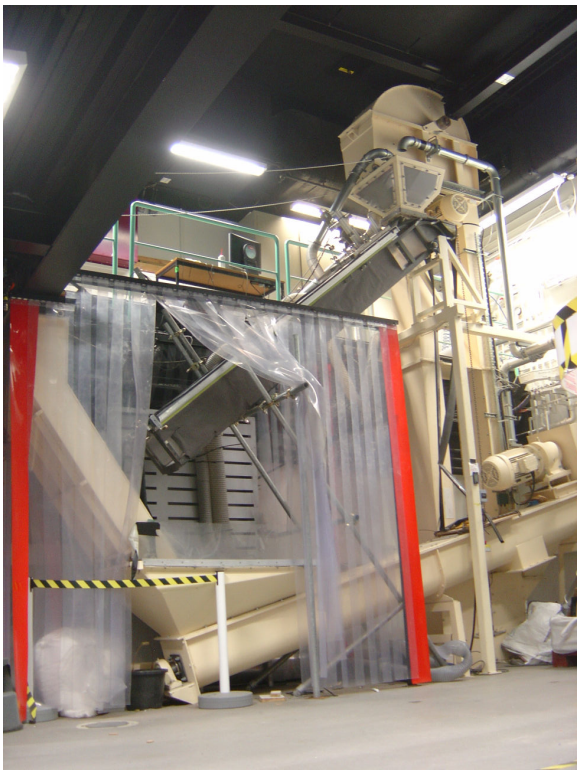

FIGURE 2. Photograph of the apparatus

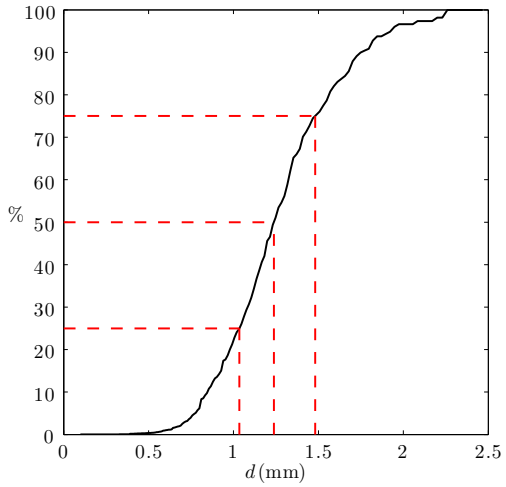

(a)

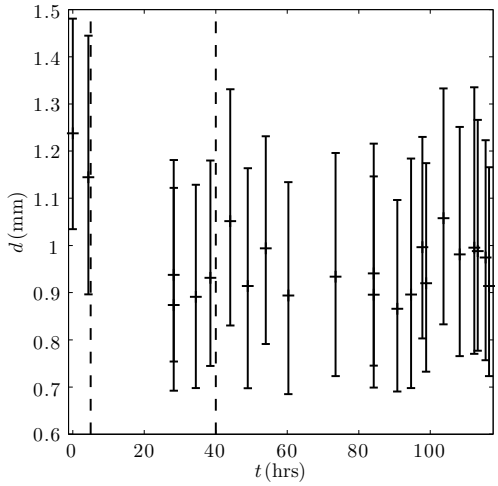

(b)

FIGURE 3. Properties of new sand. (a) Cumulative distribution function weighted by volume. Median diameter is 1.24 mm. Measured using single particle optical sizing (SPOS). (b) Distribution of particle diameter over time. Median diameter shown with error bars signifying the upper and lower quartiles. Dashed lines signify times at which new sand was added.

We measure h_{stop} as in the first method introduced in Pouliquen (1999). A flow is started with constant mass flux; when this has reached a time-steady state, the mass source is suddenly removed by shutting the gate. This allows the flow to slow down while gradually decreasing in height until it stops, leaving behind a static layer.

The $h_{\text{stop}}(\theta)$ curve has been shown to follow the phenomenological curve discussed in MiDi (2004)

$$h_{\text{stop}}(\theta) = B\frac{\mu_2 - \tan(\theta)}{\tan(\theta) - \mu_1}, \tag{3.1}$$

where the constants B, μ_1, and μ_2 are dependent on the material and on the basal condition. The constants μ_1 and μ_2 are interpreted as the upper and lower limits of

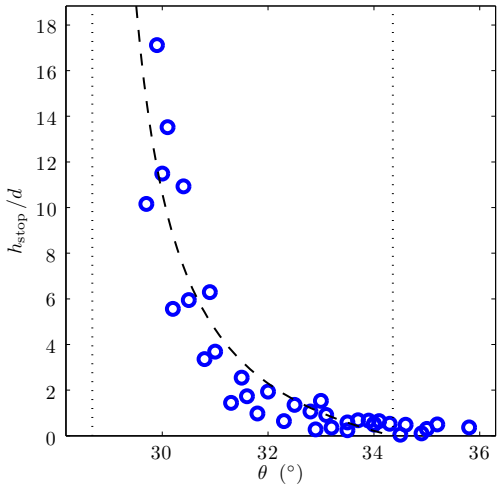

FIGURE 4. h_{stop}/d as a function of the inclination over the bumpy base. Fitting gives the $\mu_1 = 0.54$ and $\mu_2 = 0.68$.

the material's internal friction for a given basal surface. Fitting equation (3.1) to the data in figure 4 gives $\mu_1 = 0.54$ and $\mu_2 = 0.68$ for our material over the bumpy base. Measurements for h_{stop} on the flat base gave a very narrow range for the friction angles, with $\mu_1, \mu_2 = \tan(24.4° \pm 0.2°)$. At this point it is not clear if these limits of the friction coefficient are the same as in a flowing configuration, particularly for inclinations above $\tan^{-1}\mu_2$.

The density of each particle was $\rho = 2660\,\mathrm{kg\,m^{-3}}$.

3.2. *Initial Conditions and Mass Flux*

For bins and hoppers, the outflow is primarily a function of the exit geometry (Nedderman *et al.* 1982). In the experiments presented here, the flux, q, is controlled by the rectangular aperture at the bottom of the hopper, as described above. The maximum mass flux of $20\,\mathrm{kg\,s^{-1}}$ is attained at an aperture length of around 0.1 m. In order to avoid the effects of hysteresis in the hopper and to ensure that a repeatable state is achieved for each run, the same startup routine is followed each time: empty the hopper, select the aperture size and slowly fill up the hopper to the overflow. Dimensional analysis suggests that the flux will vary as

$$q \sim \rho u w l \tag{3.2}$$

for some characteristic velocity u at the aperture. Since the particles are in free fall whilst exiting the hopper, the velocity is expected to scale as if it is accelerated by gravity over a distance comparable to l, that is $u \sim \sqrt{gl}$, and therefore

$$q \sim \rho\sqrt{gl}wl. \tag{3.3}$$

The mass flux was recorded by placing a large bag attached to a crane scale and data logger under the end of the chute and measuring the bag's contents as a function of time. The derivative of this curve gives the flux, q. The plot of the scaled flux, $\hat{q} = q/\rho w\sqrt{gl^3}$ in figure 5(a) shows that the scaling law described by equation (3.3) accurately captures the functional dependence of the flux q upon the aperture length l. For large aperture lengths, $l > 59\,\mathrm{mm}$ the flow enters a slightly different regime within the hopper where the value of $\hat{q}$ alters slightly. The dependence of the mass flux q on humidity and particle

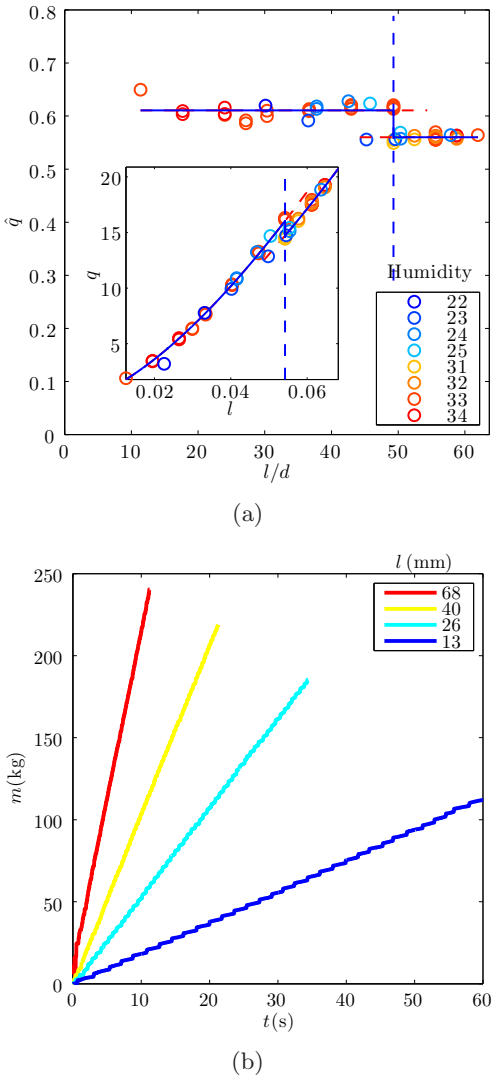

FIGURE 5. Mass flux properties. (a) Non-dimensional mass flux $\hat{q} = q/\rho w\sqrt{gl^3}$ as a function of aperture opening l. (b) Variation of mass flux over time for different aperture openings.

degradation has been checked and the effect is negligible. As the flow in the chute is independent of the conditions within the hopper, it allows q to be calibrated against l once and the fit curve to be used for all subsequent experiments. Figure 5(b) shows that the mass flux out of the hopper over time is constant over intervals larger than the data logger's sampling time of 0.1 s. The uncertainty in the rate calculation was under 1%. To ensure a symmetric initial condition, a small step of height 30 mm is placed at the top of the chute, which slows and spreads the particles evenly over the entire width.

3.3. *Boundary Conditions*

The flow is bounded by two side walls, the basal surface and the ambient air at the free surface. The sidewalls are the same for all experiments and are made of perspex whose surface has been allowed to erode to a steady state. These walls exert a frictional stress

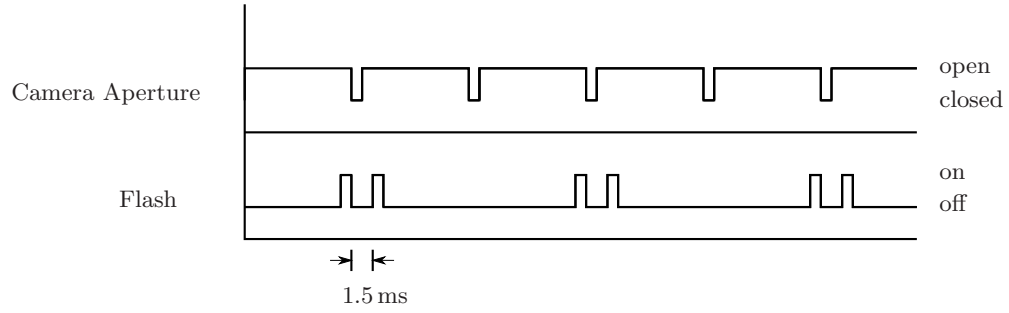

FIGURE 6. Frame Straddling, a technique developed for time-steady flows allowing for an increase in temporal resolution using standard photography equipment.

with coefficient $\mu_w = 0.45$, thus permitting a slip velocity. This has been measured by conducting an h_{stop} experiment with the perspex as the basal material. Two different basal surfaces were used, a flat surface identical to the sidewalls and a coarse sandpaper with a median grain diameter of 0.5 mm. The latter enforces a no slip boundary condition for shallow angles, but some slip occurs at high particle velocities.

3.4. *Instrumentation*

The chute is equipped with two measurement systems: one to measure surface velocity and the other flow thickness. Surface velocity measurements are calculated using Particle Image Velocimetry (PIV). The images for this are obtained from a JAI CL M4+ camera and a BitFlow R3 frame grabber. The frame rate of the camera is limited to 24 fps, so in order to minimise streak and obtain a suitable interval between frames for accurate measurements a frame straddling technique has been developed. Four banks of high-powered LEDs illuminate a section of the chute at the end of one frame and at the beginning of the next for approximately 1.5 ms. The interval between the flashes is around 1.5 ms. A pictorial representation of the synchronisation between shutter and flash can be seen in figure 6. The Particle Image Velocimetry technique developed by Sveen & Dalziel (2005) is then employed to cross-correlate the pairs of images and to extract the velocities of the particles. This procedure produces a grid of 69 by 51 velocities in both the x direction (u) and the y direction (v). This corresponds to a velocity field with a spatial resolution of approximately 3.5 mm. Since the algorithm utilises sub-pixel detail and typical displacements are of the order 5 pixels between frames, the error in the velocity measurement is estimated to be less than $0.1\,\mathrm{m\,s^{-1}}$. Around 50 pairs of images are taken for each position on the slope which are then averaged over time and along the x direction to give the cross-chute velocity profiles seen in figures 9(a) and 9(b).

The height of the flow is measured by a Micro Epsilon LLT2800-100 laser triangulator. This equipment is pre-calibrated, and gives an absolute distance from the flow surface to the CCD within. It records 100 points per profile at a rate of 400 profiles per second. This gives the surface height at a resolution of around 1 mm between points. At each of 12 positions down the slope, data are recorded for approximately 10 seconds, with the laser sheet oriented either parallel or perpendicular to the flow. No significant difference in the mean flow height was seen between orientations. This set-up gives the average flow height within 0.2 mm which is significantly less than the median grain diameter. The central 120 mm of the flow are measured, and the height within a profile typically varies by less than two grain diameters. Care must be taken when defining the height of the surface as saltating particles can obscure the dense region below. If the particles get too

close to the CCD and are out of the depth of field, then no data is recorded. The height data presented here have been time-averaged profiles.

The triangulator is also used to calibrate the PIV measurements by taking a series of photographs of a chequered pattern at different heights. The pixel coordinates of points in the pattern are matched to real world coordinates, thus removing the effects of lens distortion and parallax from the velocity calculation.

3.5. *Data Preparation*

In order to study the acceleration of the flow it is necessary to calculate the derivative of the velocity data. Doing this directly amplifies noise, so the data is first fitted with the form in equation (3.4). Median averaging of the surface velocity was chosen in order to neglect the effect of outliers. The functional form used for the fit is

$$u^2 = u_0^2 + \frac{\beta}{\kappa}\left(1 - e^{-\kappa x}\right) \tag{3.4}$$

for some constants u_0, β and κ. This satisfies the equation

$$u\frac{\partial u}{\partial x} = \frac{1}{2}\left(\beta - \gamma\left(u^2 - u_0^2\right);\right), \tag{3.5}$$

which is a linearisation of the momentum equation (2.3) in terms of the kinetic energy $E = u^2/2$. This form can represent convergence to a constant velocity state for large κx as $u^2 = u_0^2 + \frac{\beta}{\kappa}$. For positive κ this velocity is that which would be attained in an infinitely long chute, barring any phase transition. Constant acceleration (or deceleration) is also captured for small κx since $u^2 = u_0^2 + \beta x + O\left((\kappa x)^2\right)$. This fitted all of our data for appropriate choices of u_0, β and κ. Many other choices would doubtless also have worked without affecting our results. Using this fit, the total friction μ is given by

$$\mu = \tan\theta - \frac{\beta}{2g\cos\theta}e^{-\kappa x}\left(s_2 - \frac{1}{\mathrm{Fr}^2}\right) \tag{3.6}$$

where s_2 is given by a Bagnold profile for the bumpy base and a plug flow for the flat base. The height data was also fitted using a similar functional form that replaces u^2 with h. The results of the fit can be seen as solid lines in figures 11(a)–11(d).

4. Results

We observed a number of different flow regimes besides the fully dense regime that we were expecting. The phase diagrams in figure 7 show the character of the flows as the inclination θ, and the mass flux q change. The mass flux has been non-dimensionalised using the scaling $\rho w d\sqrt{gd}$.

Figure 7(a) shows that over the flat base two regimes were observed. At a fixed inclination and for a sufficiently high mass flux the flows were dense and accelerating, however for slightly lower mass fluxes an instability occurred whereby the flow detached from the walls into a dense core flanked by dilute regions (pictured in figure 8). This will be discussed further in section 4.2. The majority of flows on the bumpy base also fell into one of these two regimes. The bumpy surface also produced a number of regimes not seen on the flat base (figure 7(b)). For flows over the lowest inclinations, the velocity was constant down the slope. Of these steady, fully-developed flows, sufficiently high mass fluxes produced a superstable heap at the base (Taberlet *et al.* (2003)) and the chute quickly overflowed. No constant velocity flows were observed for the flat base, as the friction angle on the flat base was lower than the lowest inclination investigated. For the

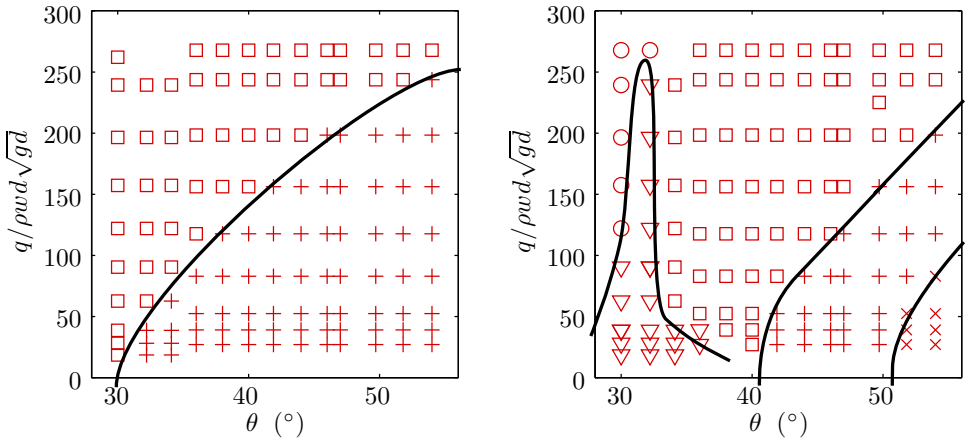

(a) Flat Base (b) Bumpy Base

FIGURE 7. Phase diagram for flows over bumpy and flat bases. (▽) Constant velocity flows, (□) Accelerating, Dense Flows, (+) Flows with separation at walls, (×) Low density flows, (○) Superstable heap formation

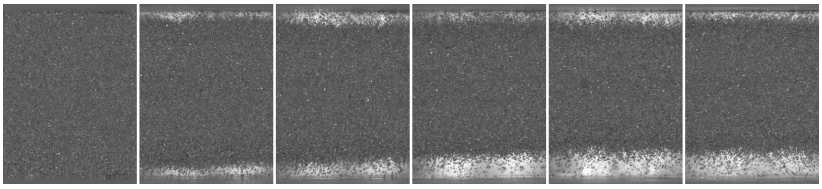

FIGURE 8. Transverse separation. Adjacent panels are separated by 0.25 m. Increasing x from left to right

highest inclinations and for low mass fluxes, a low-density regime was observed whereby the entire flow became agitated. These flows did not have a well-defined surface and so PIV and height data were not available. The flows discussed here, unless otherwise specified, lie in the dense, accelerating regime. We did not notice any bistable regimes though we did not look for these in detail.

4.1. *Fully Dense Flow*

The flows over flat bases showed higher average surface velocities than over bumpy bases, which is to be expected since a flat surface gives less resistance. The typical surface velocity profile development for each base can be seen in figure 9. Each line represents a time averaged velocity profile at a given point on the slope. For both flows depicted it can be seen that the material is accelerating as it progresses down the slope.

A striking result was the effect of the basal surface on the shape of the velocity profile at the free surface. Figure 9 shows flows with the same control parameters (q, θ) exhibiting qualitatively different surface profiles. Flows over the flat bases invariably had a profile with a gradual and continuous change in velocity gradient across the chute, whereas the flows over the bumpy base developed a plug region in the centre of the chute. The plug region is flanked by sheared regions near the walls, with the velocity varying linearly with distance from the wall. Flows over both of these surfaces exhibit a non-constant acceleration.

The insets of figure 9 show each velocity profile normalised by its peak velocity. In

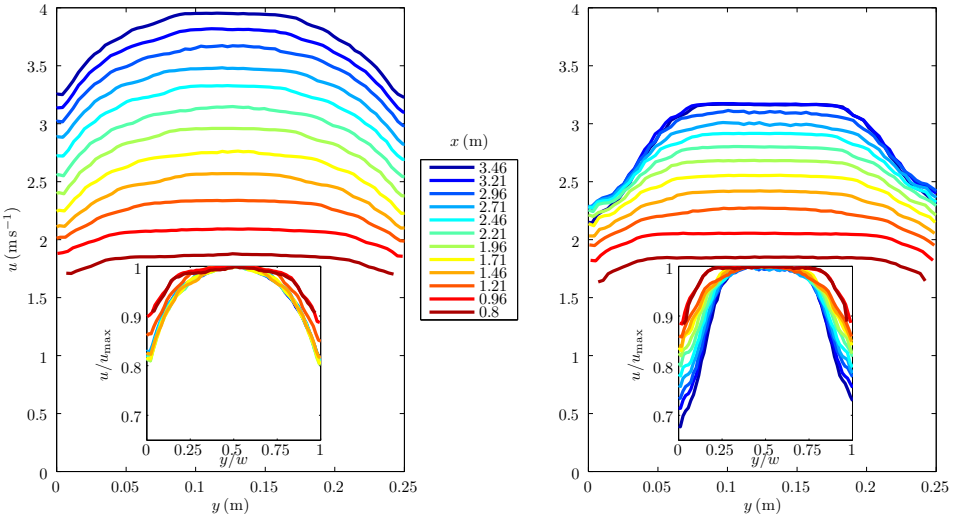

(a) Flat Base (b) Bumpy Base

FIGURE 9. Evolution of the time-averaged transverse velocity profile as the material accelerates down the slope. The flow parameters are $\theta = 40^\circ$ and $q = 19.1\,\mathrm{kg\,s^{-1}}$. Inset shows $\frac{u}{u_{\max}}$ against y/w.

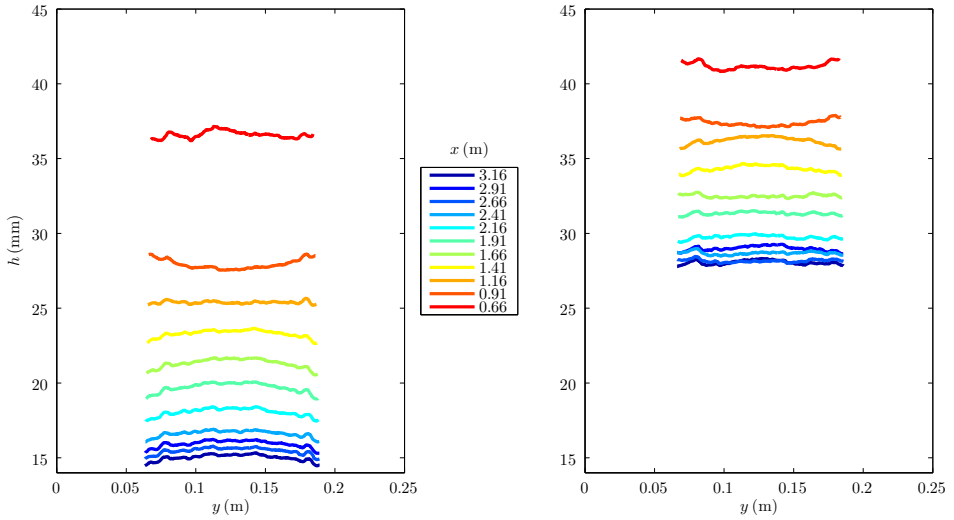

(a) Flat Base (b) Bumpy Base

FIGURE 10. Evolution of the time-averaged transverse height profile as the material accelerates down the slope. The flow parameters are $\theta = 40^\circ$ and $q = 19.1\,\mathrm{kg\,s^{-1}}$. No height data was available at the edges.

the flat case, the effect of the shape of the initial condition is transient over a distance of around 1.5 m after release. After this point, the shape of the profile remains steady in time, implying the y dependence of f is constant. In the bumpy case however, the slip velocity at the wall tends to a limit while the central, plug-flow region carries on accelerating implying a non-self-similar shape and therefore the s_n change as the flow develops.

Figure 10 shows the height evolution for the same flows as figure 9. The variation of the height across the slope is minimal, typically less than $2d$. Height data for the edges of the flow were not systematically available due to the limited width of the laser sheet, however, the edges were checked periodically and showed no significant deviation in height from the centre. As the flow accelerates down the slope, conservation of mass causes the height to decrease. The surface velocities over a bumpy base are typically lower and, by this principle, the flow is deeper for the same q over the flat base.

Flows for which $\theta < \theta_2$ showed no acceleration along the chute, maintaining constant velocity and height throughout. No non-accelerating flows were observed for flows over the flat base as the $\theta_{1,2}$ were outside of the investigated range.

For the accelerating flows, though the cross slope velocity profiles are qualitatively different between the bases, there is no qualitative difference in the development of u_s down the slope. Comparing figure 11(b) to figure 11(a) and figure 11(d) to 11(c) we see the same general behaviour from both surfaces: gradually changing acceleration accompanied by the reduction in flow height enforced by mass conservation. For both surfaces we see a general trend of increasing velocity for both increasing q and θ. The third column in figure 11 plot the volume fraction multiplied by the shape parameter s_1 calculated using the expression $q = \rho\phi s_1 whu_\mathrm{s}$. This, in all cases, is in the range 0.3–0.7. A Bagnold profile has $s_1 = 3/5$, so for a typical volume fraction of $\phi = 0.6$ we should expect to see a value $\phi s_1 = 0.36$, and we do for the bumpy base, indicating that the Bagnold profile assumption is reasonable in the calculation of the friction coefficient. Higher values of $s_1\phi$ indicate the presence of some slip developing at the basal surface.

For plug flows $\phi s_1 = 0.6$ which is closer to the value seen on the flat base. However, values seen in figures (c) and (a) show that the observed values are slightly lower than predicted, indicating that some curvature is present in the z direction and the basal slip velocity is therefore less than the mean surface velocity, as is to be expected as the plug-like profile is a zeroth order approximation of the flow. Variation in ϕs_1 down the slope is small.

The different bases produced different behaviours with respect to the bulk friction coefficient. For the bumpy base, a Bagnold depth dependence has been assumed in the calculation of μ in equation (2.6). The precise choice of depth dependence does affect the calculated value slightly. The difference in s_2 at extremes of Bagnoldian and plug flow is a factor of approximately 2, we may safely say that the deviation of μ from the equilibrium value of $\tan\theta$ can at most be affected by this much. However, the qualitative behaviour remains unchanged by the depth dependence. Figure 12(a) shows that on a bumpy base, μ varies from around 0.55 to 1.1. The inset of figure 12(a) shows that the ratio $\mu/\tan\theta$ is less than the steady-state value of 1 for all flows, and no lower than around 0.8. The very lowest values of μ are attained for low inclinations, where the flows are steady. The friction balances gravity in these flows despite the inclination being above the angle of maximal resistance θ_2, as the sidewalls give an extra frictional contribution. At higher inclinations, we see a dependence on q appearing: the lower the value of the flux q, the lower the bulk Fr and the smaller the range of μ down the slope. For a given Froude number and inclination the highest values of μ are seen for the flows with smaller flow heights, this can be attributed to increase in resistance caused by the flow having to dilate more near a boundary in order to flow (Pouliquen 1999).

Figure 12(b) shows that on a flat base, there is only a weak variation of $0.5 < \mu < 0.6$ over all Fr. This is slightly larger than the maximal friction angle obtained from the h_stop measurement of $\mu = 0.45$. This disparity is possibly due to the addition of wall friction. The flux dependence over the flat base is more complicated than for the bumpy base, and is discussed in section 6.

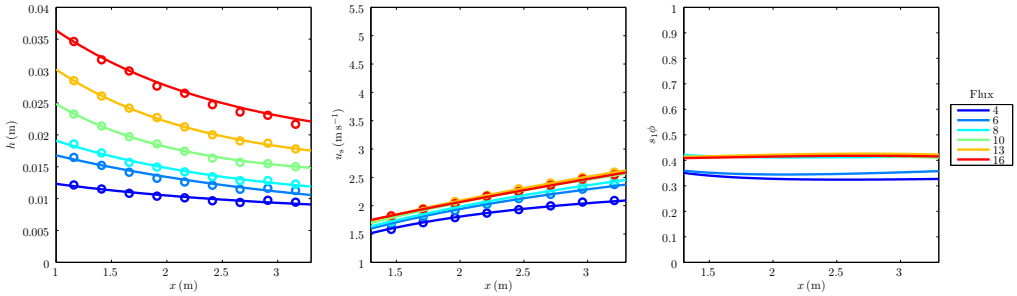

(a) Varying flux at $\theta = 32.2°$ on the flat surface.

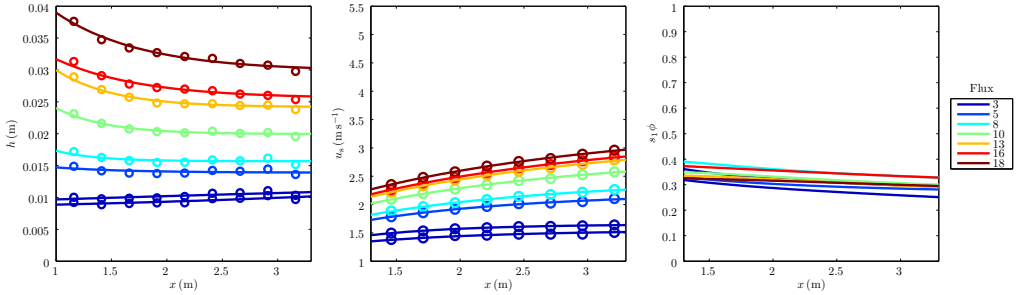

(b) Varying flux at $\theta = 38°$ on the bumpy surface.

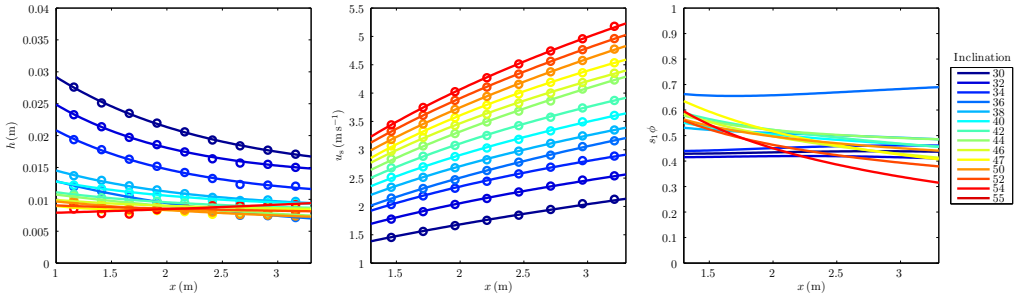

(c) Varying inclination for $q = 11\,\mathrm{kg\,s^{-1}}$ on the flat surface.

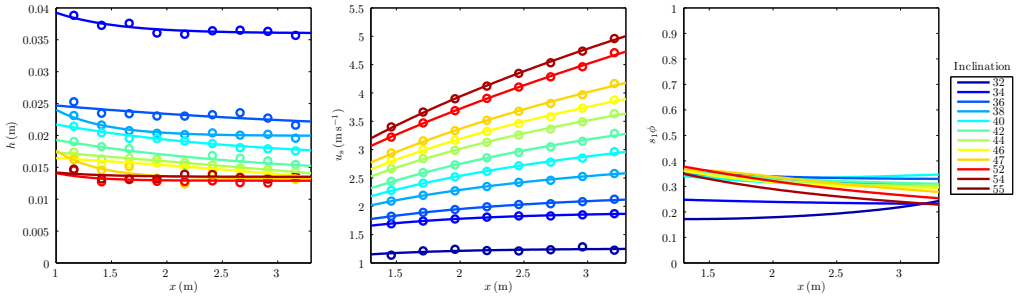

(d) Varying inclination for $q = 11\,\mathrm{kg\,s^{-1}}$ on the bumpy surface.

FIGURE 11. Effect of varying q and θ on the two bases.

Figure 13 shows the velocity of the material at the end of the chute as a function of the inclination θ. The exit velocity for a given inclination is a monotonically increasing with the flux, and is reflected in the decreasing value of μ as the flux increases. This cannot be collapsed by scaling with the flux q because if friction is the only force limiting the

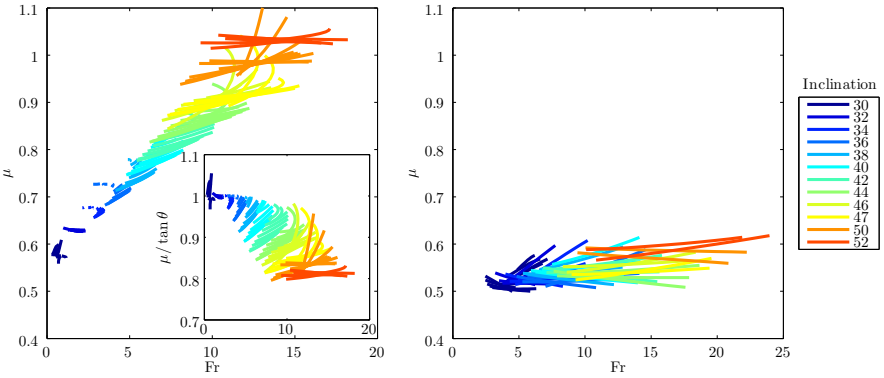

(a) Bumpy base (b) Flat base

FIGURE 12. μ as a function of Fr. Coloured by inclination. A Bagnold depth dependence is assumed for flows over the bumpy surface, and a plug flow for the flat surface. Inset shows μ divided by the value attained for a non-accelerating flow, $\tan\theta$.

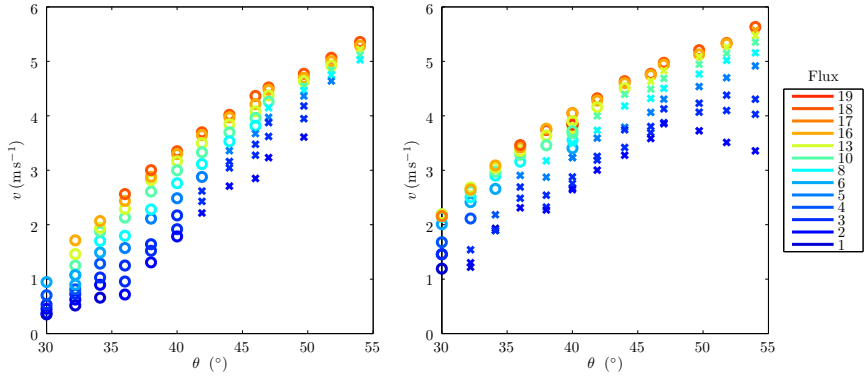

(a) Bumpy Base (b) Flat Base

FIGURE 13. Velocity at the end of the chute as the inclination θ and the flux q vary. Flows that are dense across the entire width are denoted by ($\circ$), and flows that have undergone transverse separation are denoted by ($\times$).

velocity then eventually $u \propto \sqrt{x}$, independent of q. Setting μ as a constant in equation (2.3) and assuming Fr is large at equilibrium we integrate to obtain

$$\frac{1}{2}u_s^2 = \frac{1}{s_2}\left(\sin\theta - \mu\cos\theta\right)xg + \frac{1}{2}u_0^2, \tag{4.1}$$

for some constant u_0. This expression is independent of q, and therefore we cannot collapse the data for different fluxes.

4.2. *Transverse Separation*

When the flows are sufficiently energetic a dilute, high granular temperature region forms at the walls that flanks a dense core. For a given inclination, the value of q at which this occurs is lower on a flat base than the bumpy base. This is possibly due to the bumpy base dampening the high energy particles at the boundary. Since the interaction with the boundary in this regime is different to that of the fully dense flows, a direct comparison in terms of μ becomes meaningless, and so these experiments have been excluded from figure 12(b).

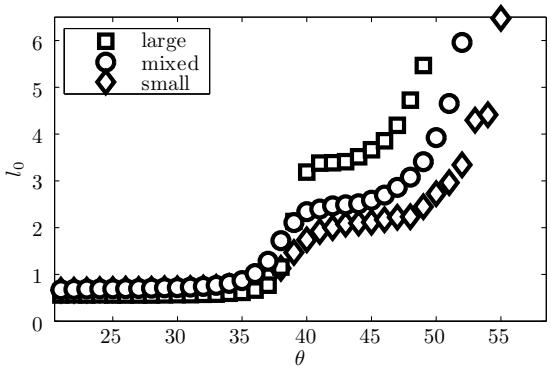

FIGURE 14. Height of the low density layer at the basal surface in DEM simulations allowed to reach a fully developed state. Small particles have radius 0.8, large particles have radius 1.2, and mixed consists of an equal volume of each particle type.

The data denoted by crosses in figure 13 show the values of θ and q for which the flow visibly separated from the walls before the material exits the chute. At a fixed inclination, the separation disappeared for sufficiently high mass fluxes. This phenomenon is analogous to the 2D numerical simulations performed by McNamara & Young (1994), where a dense region appears and is contained by boundary regions that have a high granular temperature and low volume fraction. Similar effects have been reported in numerous other situations (see Goldhirsch 2003). Figure 8 shows the development of the collapse of a flow over a flat base. The flow invariably starts attached to the walls and detaches once there is sufficient agitation of the grains at the boundary. The width of the high density region in the centre of the chute decreases and appears to tend to a limit. For sufficiently high inclinations and low mass fluxes the agitation of the grains is large enough for the entire flow to be in the dilute regime (see figure 7). These very energetic flows over the bumpy base ($\theta > 52^\circ$, $q \lesssim 2\,\mathrm{kg\,s^{-1}}$) have been excluded from figure 12(a) as the saltating particles form an ill-defined surface, and hence data is not available.

This low-density effect can also take place at the basal surface. On a bumpy base this manifests itself at high inclinations ($> 46^\circ$) and the effect can be seen through the total friction, μ. When the separation occurs, μ is relatively small when compared with lower inclinations (see figure 12(a)), and also becomes independent of the Froude number and the mass flux.

The thickness and character of this basal layer is governed by a complicated dependence on other flow parameters. DEM simulations were also performed to investigate this. A soft particle model was used with a damped linear spring for the normal force (coefficient of restitution 0) and Coulomb friction for the tangential force (coefficient of friction 0.5). Particle stiffness was chosen so that the maximum overlap was less than 1%. The time step was 1/10 of the binary collision time. Particles of radius 0.8 and 1.2 were simulated in three combinations, all small, all large or mixed equally by volume fraction. The base was made of an equal mixture of large and small particles held at fixed positions taken from another simulation where a thick layer was allowed to form randomly. The simulations were allowed to evolve until equilibrium was reached and then the results recorded until flat profiles were obtained. The density profile was analysed by fitting the regularised step function

$$\phi(z) = \frac{1}{2}\left[\tanh\left(\frac{z - z_0}{l_0}\right) - \tanh\left(\frac{z - z_1}{l_1}\right)\right],$$

which gave a very good fit in all cases. The width of the bottom layer l_0 is shown in figure 14 where one sees a very strong dependence on the inclination. At the base, a low density shear layer of thickness l_0 supports a high density passive overburden. For all particle species, the thickness was shown to be monotonically increasing in the slope angle. There are two transition points that can be seen, one where the layer first separates from the base, and a second one above which the height of the layer increases rapidly with inclination until the entire flow becomes diffuse and kinetic. This density inversion phenomenon and the velocity independence of the friction coefficient has also been reported experimentally in Taberlet *et al.* (2007). However, in contrast to Taberlet *et al.* (2007) such flows were seen for high inclinations, far above θ_2, indicating that a much larger energy input is needed for our material to maintain a supported state, possibly due to the increased rolling resistance and therefore dissipation afforded by the irregularity of the particles' shape.

4.3. *Surface Waves*

Shallow flow systems are subject to instabilities known as roll waves or Kapitza waves (Forterre 2006) due to the tendency of deeper regions to move faster. This is typified by the flow rule in equation (1.1). For the flows investigated here, these waves occurred at angles near θ_2 for moderate flow rates. The space-time plot in figure 15 shows the amplitude of the waves on a slope of 32.2° at a mass flux of $5.9\,\mathrm{kg\,s^{-1}}$. The time-averaged height has been subtracted at each position, and the general trend of decreasing height as the flow develops down the slope is apparent. The colour difference has been normalised such that white corresponds to a 5 mm deviation above the mean height and black represents a 5 mm depression. Waves appear soon after exiting the hopper with an amplitude of around 2–3 mm and a wavelength of 404 mm. Half way down the slope, at 2.05 m after release, the amplitude has increased by a factor of two and the wavelength has increased slightly to 564 mm. The last reading, which shows little surface variation, would suggest that the flow has crossed some threshold and the disturbance has been neutralised. The linear theory presented in Forterre & Pouliquen (2003) gives a stability threshold of $\mathrm{Fr} \gtrapprox 0.7$, above which the flow is susceptible to these surface waves. The phase speed of the waves is in agreement with the velocity calculated using PIV to within 5%.

4.4. *Convection Currents*

Figure 16 shows typical behaviour for the horizontal velocities at the surface of a flow over a bumpy base. There is a down-welling at the walls which is accompanied by an up-welling around 2 cm toward the centre, reminiscent of wall-cooling. Such patterns have been observed before but they are contrary to the inferred flow field in studies such as Savage (1979).

4.5. *Longitudinal Vortices*

Figure 17 shows the flow over a bumpy base with $\theta = 40°$ and $q = 5.5\,\mathrm{kg\,s^{-1}}$. Approximately 3 m after the sand is released, peaks in the downstream velocity develop similar to those seen by Börzsönyi *et al.* (2009) and Forterre & Pouliquen (2001).

5. Numerical Solution and Comparison with $\mu(I)$ Rheology

A first order finite volume code has been developed to investigate the rheology presented in Jop *et al.* (2006) in an accelerating regime. This rheology has received a lot of interest recently but has only been tested for values of I that are typically low ($\lessapprox 0.5$)

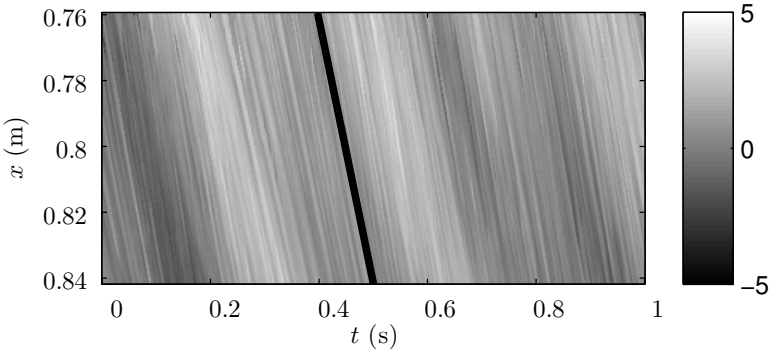

(a) $x = 0.80\,\mathrm{m}$, $v = 0.80\,\mathrm{m\,s^{-1}}$, $h = 0.047\,\mathrm{m}$, $\mathrm{Fr} = 1.35$

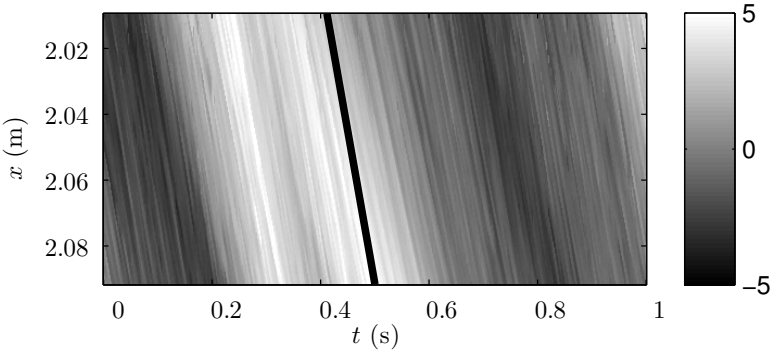

(b) $x = 2.05\,\mathrm{m}$, $v = 0.93\,\mathrm{m\,s^{-1}}$, $h = 0.037\,\mathrm{m}$, $\mathrm{Fr} = 1.68$

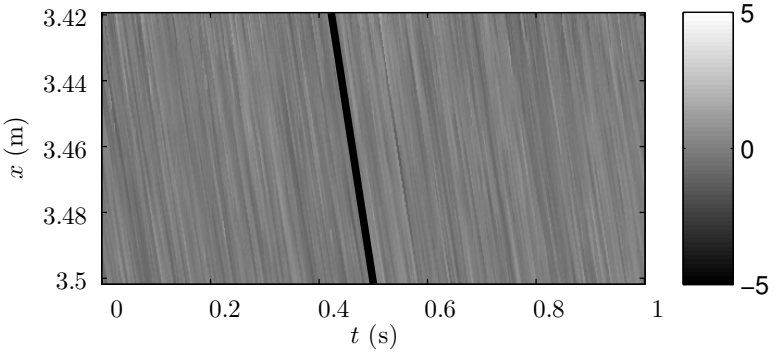

(c) $x = 3.46\,\mathrm{m}$, $v = 1.06\,\mathrm{m\,s^{-1}}$, $h = 0.030\,\mathrm{m}$, $\mathrm{Fr} = 2.18$

FIGURE 15. Variation in height at $\theta = 32.2^\circ$ $q = 5.9\,\mathrm{kg\,s^{-1}}$. The colour represents a deviation about mean in mm. The black lines indicate the calculated velocity from PIV measurements, showing that the waves move with the same velocity as the particles

and only for non-accelerating flows. This rheology assumes an isotropic pressure and a constant density. Experimental evidence in Pouliquen *et al.* (2006) suggest that some variation in ϕ will occur in regions of high I, but the dependence is rather weak so we ignore this. The flow is observed to be flat across the slope so can neglect $\dfrac{\partial P}{\partial y}$ and as-

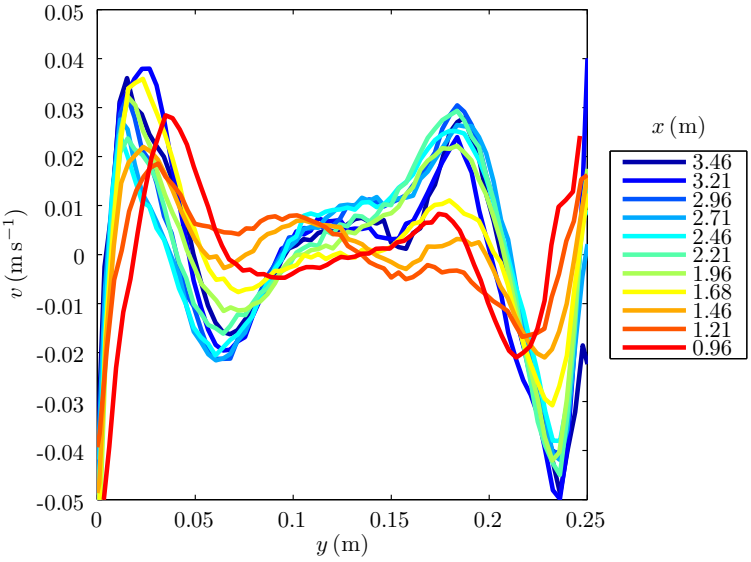

FIGURE 16. Horizontal velocity for a flow on a bumpy base with $\theta = 44^\circ$ and $q = 13\,\mathrm{kg\,s^{-1}}$

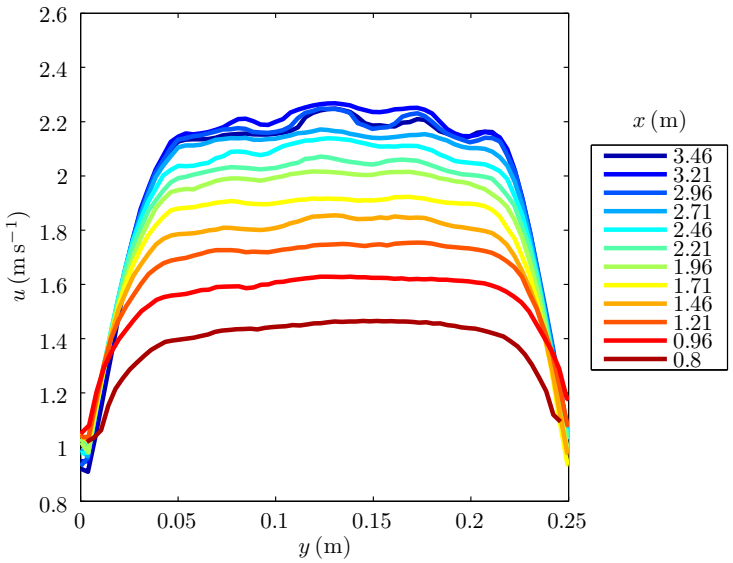

FIGURE 17. The formation of longitudinal vortices on a bumpy base with $\theta = 40^\circ$ and $q = 5.5\,\mathrm{kg\,s^{-1}}$. The height decreases monotonically from 17 mm at the top of the chute to 11 mm just before the exit.

sume that cross-slope velocities are zero. Down the slope the height varies by at most 20 mm over 2 m so the ratio of $\dfrac{\partial P}{\partial x}$ to gravitational acceleration and friction is of order $\dfrac{\partial h}{\partial x} = O(1/100)$ so we neglect this. If we again consider the surface height to vary from 40 mm to 20 mm over 1 s this gives a vertical strain rate of order $\dfrac{\partial w}{\partial z} = 1\,\mathrm{s^{-1}}$. Because of

incompressibility this must of course match the downslope strain rate $\dfrac{\partial u}{\partial x} = 1\,\mathrm{s}^{-1}$ (corresponding to a change of $2\,\mathrm{m\,s}^{-1}$ in $2m$). These seem like large strains but we neglect them because in the $\mu(I)$ rheology these contribute to the deviatoric stress after being divided by the total strain. This is dominated by $\dfrac{\partial u}{\partial z}$, which for these rapidly accelerating flows could be given by a flow of $4\,\mathrm{m\,s}$ and $40\,\mathrm{mm}$ thick corresponding to a strain rate of $100\,\mathrm{s}^{-1}$. Thus the only stress components we consider are σ_{xy} and σ_{xz} since all others are $(1/100)$. Taking the velocity to be $\boldsymbol{u} = (u, 0, 0)$, then the conservation of momentum of a time-steady flow is given by

$$\rho\phi\left(u\frac{\partial u}{\partial x}\right) = \rho\phi g\sin\theta + \frac{\partial\sigma_{xy}}{\partial y} + \frac{\partial\sigma_{xz}}{\partial z}. \tag{5.1}$$

Since we are taking h constant across the slope the depth and width integrated conservation of mass equation is

$$\rho\phi w\frac{\partial h\bar{u}}{\partial x} = 0, \tag{5.2}$$

therefore $h\bar{u} = \text{const.} = q/\rho\phi w$. Rearranging gives $\bar{u} \propto h^{-1}$ as is a function only of x. The stress tensor is defined by

$$\sigma_{ij} = -P\delta_{ij} + \tau_{ij} \quad \text{and} \quad \tau_{ij} = \mu_i(I)P\frac{\dot{\gamma_{ij}}}{|\dot{\gamma}|} \tag{5.3}$$

where the $\dot{\gamma}_{ij} = \partial_i u_j + \partial_j u_i$ are the components of the strain tensor and $|\dot{\gamma}_{ij}| = \sqrt{\dot{\gamma}_{ij}\dot{\gamma}_{ij}/2}$ is the local strain rate.

Solving the z component of the momentum equation in the long wave approximation (Gray *et al.* 1999) gives hydrostatic pressure $P = \rho\phi g z\cos\theta$. In this rheology, $\mu_i(I)$ takes the form shown in equation (1.3), with the three parameters taken from h_{stop} measurements and a typical value of $I_0 = 0.3$ (Jop *et al.* 2005).

The stresses induced by changing surface height enter through the term

$$\frac{\partial P}{\partial x} = \rho\phi g\cos\theta\frac{h}{u}\frac{\partial u}{\partial x}, \tag{5.4}$$

using an upper bound for the acceleration $\partial_x u < g\sin\theta/u$ and the mass conservation equation 5.2 we find we can neglect these stresses if $\mu > \mathrm{Fr}^{-2}\tan\theta$, which is the case for the flows investigated here. For the bottom surface, a no-slip boundary condition is applied while for the sidewalls a slip boundary with constant Coulomb friction is applied. The latter can be written as

$$\sigma_{xy} = -\mu_{\mathrm{w}}Pu/|u|, \tag{5.5}$$

where μ_{w} is a constant taken from h_{stop} measurements over the perspex wall material ($\mu_{\mathrm{w}} = 0.45$).

Care must be taken at the free surface as the highest derivative in equation (5.1) is multiplied by zero. The equation is therefore singular and first order there, and no boundary condition is necessary. However, as $\sigma \propto P$ the surface is stress free which is the boundary condition we would normally expect to apply. This leads to the behaviour of I near the free surface being complicated and warrants further investigation. If we assume a Bagnold depth dependence near the surface then

$$\frac{\partial u}{\partial z} = \frac{I_{\mathrm{bag}}\sqrt{zg}}{d} \tag{5.6}$$

for some constant I_{bag}. If, in addition to this, there is a cross slope variation near the

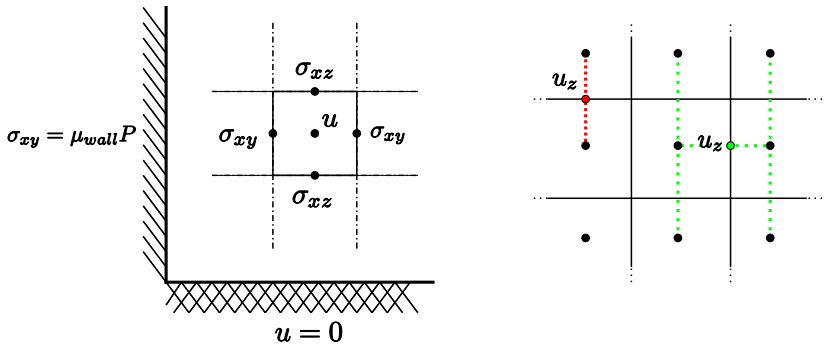

FIGURE 18. Depiction of the cell structure and differentiation schemes used in the finite volume method for solving the $\mu(I)$ rheology.

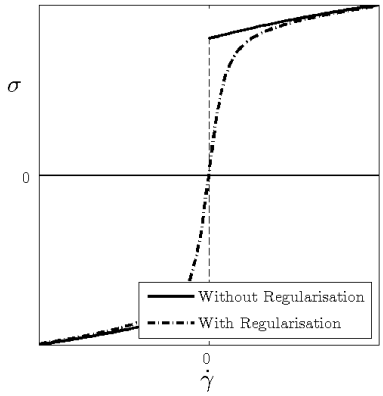

FIGURE 19. Regularisation of shear stress at zero strain.

surface then

$$I = \frac{d}{\sqrt{zg}}\sqrt{\left(\frac{\partial u}{\partial y}\right)^2 + \left(\frac{\partial u}{\partial z}\right)^2} = \sqrt{\frac{d^2}{zg}\left(\frac{\partial u}{\partial y}\right)^2 + I_{\text{bag}}^2}, \tag{5.7}$$

implying that $I \to \infty$ as $z \to 0$ at the free surface if $\partial_y u \neq 0$. The thickness of the boundary layer over which the y-variation in I decays to I_{bag} is given by

$$z = \frac{d^2}{I_{\text{bag}}^2 g}\left(\frac{\partial u}{\partial y}\right)^2. \tag{5.8}$$

We do not attempt to resolve this boundary layer in our simulation as μ_i remains finite and is multiplied by $P = 0$ at the surface, meaning that the stress remains well defined everywhere. A fixed rectangular grid, pictured in figure 18, is used to define the locations at which velocity and stress information is stored. Each velocity point is stored in the centre of a cell, with $\partial_i u$ calculated at the cell boundary using central differencing. These derivatives are then in turn centrally differenced to give the divergence of σ.

Care must also be taken in regions where $|\dot{\gamma}_{ij}| = 0$ as equation (5.3) becomes an inequality there. For such regions to start shearing, the yield stress $\tau_{ij} = \mu_1 P$, which is implicitly defined in the rheology, must be overcome. Full resolution of these areas would require tracking a yield surface and estimating ill-defined static stresses. However, as these regions are small compared to the bulk of the flow, this added complication gives a negligible increase in accuracy at the expense of considerable computational complexity.

We can therefore relax this condition by introducing a small regularisation parameter, ϵ, such that

$$|\dot{\gamma}_{ij}| = \sqrt{\left(\frac{\partial u}{\partial z}\right)^2 + \left(\frac{\partial u}{\partial y}\right)^2 + \epsilon^2}. \tag{5.9}$$

This has the effect of removing the yield stress $\mu_1 P$ and placing an upper bound on the effective viscosity of the material ($\nu_{\text{eff}} = \frac{\mu P}{\epsilon}$). As a result, a small creep velocity appears in regions that would otherwise be static. A similar procedure is followed with the wall stress to aid convergence, whereby $|u|$ is replaced with $\sqrt{u^2 + \delta^2}$.

The strong non-linearities in the problem obstruct the use of high order solvers. In particular, a pseudo-spectral Galerkin method produced solutions that degenerated into noise after a few iterations. MATLAB's `ode15s`, a first-order, multi-step, stiff ODE solver gave rapid convergence to the solution.

The approach was as follows:

(*a*) Extrapolate velocity field quadratically half a grid space to the boundaries,
(*b*) Substitute in velocity boundary conditions,
(*c*) Calculate derivative quantities and stress tensor using central differences,
(*d*) Substitute in the stress boundary conditions at the walls,
(*e*) Take divergence of the stress tensor,
(*f*) Use `ode15s` to calculate velocity field for chosen x values.

The initial condition requires specifying $u(0, y, z)$ but, experimentally, only the initial velocity at the surface $u(0, y, 0)$ can be measured. As such, the depth dependence of the velocity profile is unknown and can be treated as a degree of freedom with which to fit the numerical results to the experimental data. Experimentally, to begin with, there is little y-variation of the velocity profile. For this reason, the initial condition chosen is to be a near-plug flow with the value of the mean velocity slightly less than the first recorded experimental measurement. This was done to allow the effect of the initial condition to be minimised before the flow is quick enough for comparisons to be made to the experimental data. There is a small amount of shear introduced in the initial profile to avoid the problems of near static regions and to aid convergence. Other initial conditions based on the shape of the experimental velocity profile have also been tried, but the results are largely similar after around 1 m of travel.

Figures 20 and 21 show the internal properties of a typical flow at an inclination just above the maximum friction angle. The velocity profile in figure 20(a) agrees qualitatively with expectations — the velocity is greatest at the free surface, and decreasing toward the boundaries. The profile of I in figure 20(b) has some interesting features — there are a number of high I zones: the centre of the base, the upper portion of the side walls and the boundary layer near the free surface, where the inertial parameter is infinite (and so not plotted). Using numerical data we can use equation (5.8) to estimate the size of the boundary layer. A typical value for u_y at the surface for the simulations presented in figure 20 is 1, meaning that the boundary layer has size $z/d = 0.02$. The maximum value of u_y at the surface is higher at 44 but is concentrated very near the walls, where the assumption of a Bagnold background profile and therefore equation (5.7) is invalid. This length scale is too small to affect the grains for the size of the flows investigated here. This is to be expected as a large change in I only elicits a small change in $\mu(I)$ and σ since $\mu \to \mu_2$. This can be seen in figure 20(c). The resolution of the simulations presented here would need to increase by an order of around 100 to flatly capture the change in I over this layer.

Figure 20(d) shows the velocity field normalised by the transverse profile taken at some arbitrary depth. Since the profiles are not just constant multiples of each other, the

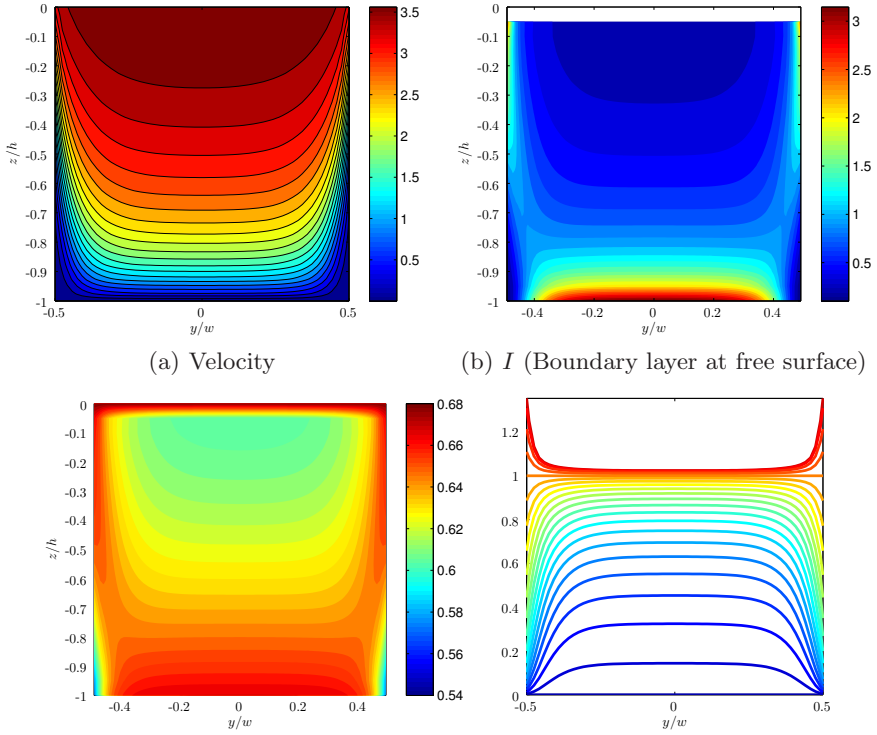

(a) Velocity (b) I (Boundary layer at free surface)

(c) Friction (d) Separability

FIGURE 20. Results of a simulation at $\theta = 38^\circ$ and q =17.8 kg s^{-1}, 3.5 m after release. The parameters used are $\mu_1 = 0.54$, $\mu_2 = 0.68$, $I_0 = 0.3$ and $\mu_w = 0.45$. The height was calculated as $h = 0.017 = 17d$.

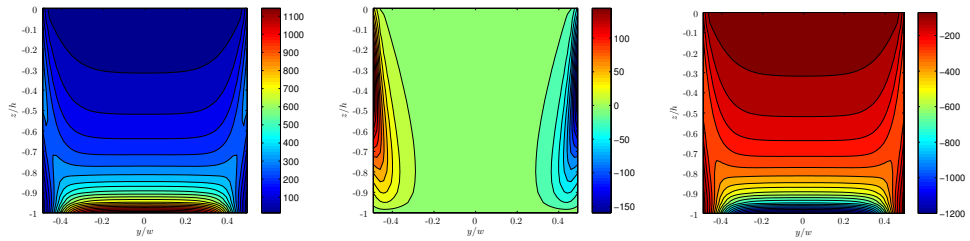

(a) $|\dot{\gamma}_{ij}|$ (b) $\dfrac{\partial u}{\partial y}$ (c) $\dfrac{\partial u}{\partial z}$

FIGURE 21. Derivative quantities of simulation at $\theta = 38^\circ$ and $q = 17.8\,\mathrm{kg\,s^{-1}}$, 3.5 m after release. Same parameters as figure 20 are used.

functional form of the velocity is not separable, i.e. it cannot be represented by the form $u = U(x)f(y)g(z)$, meaning that the transverse and depth effects are intimately tied.

Figure 21 shows the flatly changing derivatives of the velocity field used in the calculation of I and the stress tensor σ. It can be seen that the largest shear occurs at the base, and so the frictional losses are highest there.

Substitution of the $\mu(I)$ rheology and the boundary condition (5.5) into equation (5.3) gives two contributions to the total friction:

$$\mu = \mu_w \frac{h}{w} + \mu_b, \tag{5.10}$$

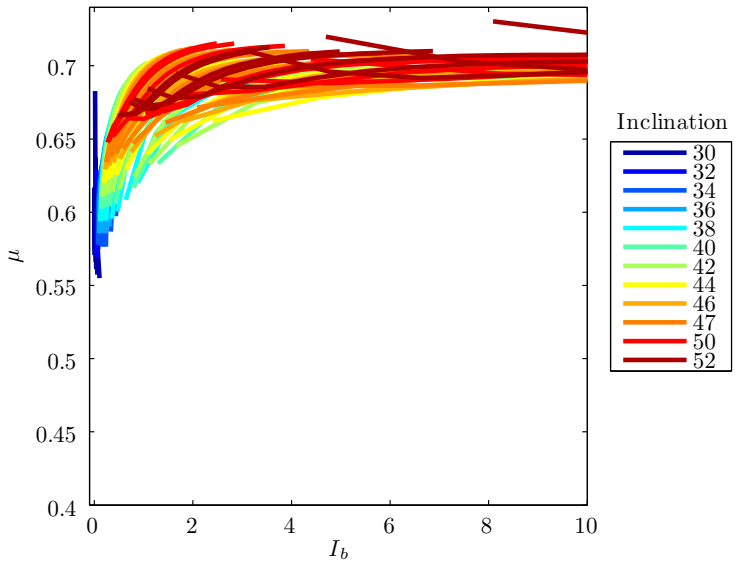

FIGURE 22. Numerical simulations of the total friction μ on a bumpy base. $\mu_2 = 0.68$, $\mu_w = 0.45$

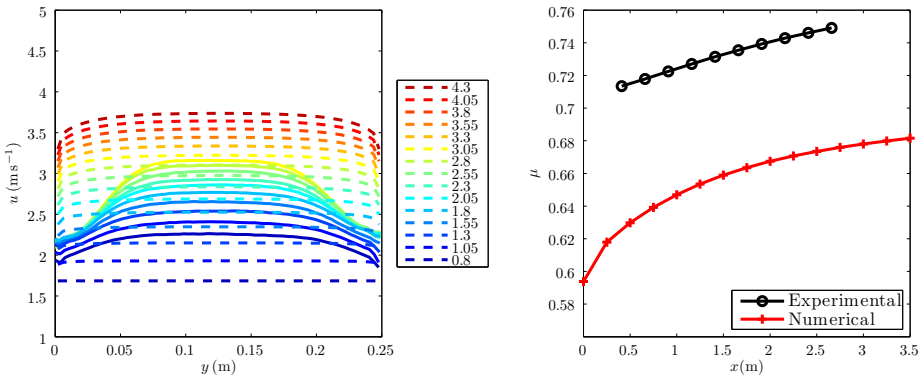

(a) Surface Velocities (b) Friction coefficient μ

FIGURE 23. Experimental and Simulation properties over a bumpy base at $\theta = 38°$ and $q = 17.8\,\mathrm{kg\,s^{-1}}$ using parameters $\mu_1 = 0.54$, $\mu_2 = 0.68 = \tan(34°)$ and $I_0 = 0.3$

where μ_w is defined as in equation (5.5), and μ_b is the effective basal friction and must therefore be in the range $\mu_1 \leq \mu_b \leq \mu_2$. This relationship specifies the total frictional resistance — figure 22 shows the total friction approaching μ_2 as the flows accelerate and get thinner. This is a behaviour not seen in the experimental results and will be discussed in section 6.

The transverse surface velocity profiles that are produced by the simulations exhibit a qualitative difference to those observed experimentally. In the simulations, there is invariably a flat change of gradient over the entire width of the chute, as opposed to the experimental profiles on the bumpy base which have three linear regions. A comparison between the numerical and experimental flows on an inclination slightly higher than θ_2 is shown in figure 23. We see that the total friction μ for the experimental data is much higher than than the total friction predicted using the $\mu(I)$ rheology.

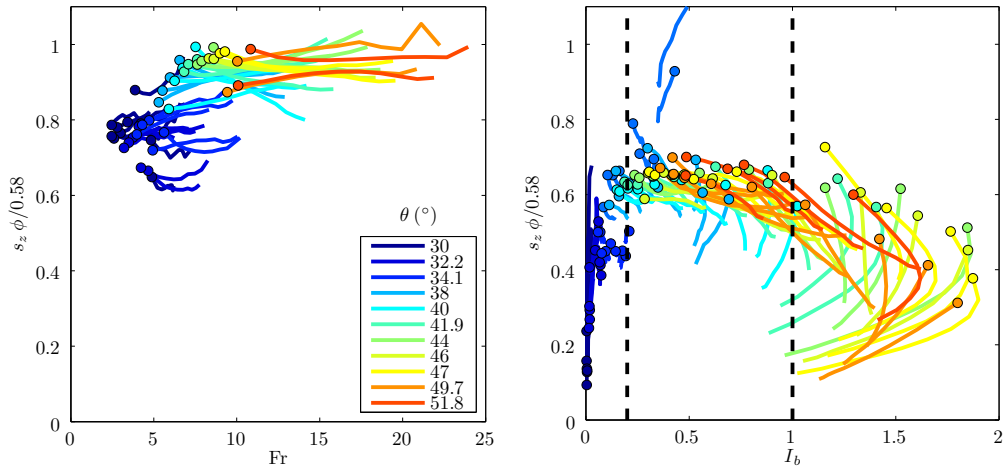

(a) Flat base (b) Bumpy base

FIGURE 24. Plot of $s_z\phi/0.58$. Coloured by inclination. The dots indicate the measurement at the top of the chute. The bumpy case is plotted against I_b, and the flat against Fr. The lines in (b) indicate the region where a Bagnold profile is likely.

For inclinations below the maximum friction angle, good quantitative agreement of the average velocity, u_s, and μ can be achieved by changing the rheological parameters from their experimental values. It is also possible to closely match the slip velocity at the wall by changing the wall friction coefficient. Any change of μ_w only has a small effect on the average velocity since its effect is weighted by the aspect ratio h/w, and can therefore be independently chosen to match the wall velocity.

6. Discussion

The $\mu(I)$ rheology has been developed and validated primarily for equilibrium flows with low I. However, we have compared it to our experiments of accelerating flows and high I, and found poor agreement with our data. One crucial difference is the existence of the limiting value of friction in equation (5.10) as the flow develops and thins. For this rheology, which takes its parameters from h_{stop} experiments, the limiting value is independent of the inclination of the flow. A comparison between the numerical results in figure 22 and the data presented in figure 12 strongly suggests that experimentally this is not true. For inclinations where $\theta > \tan^{-1}\mu_2$, the $\mu(I)$ rheology predicts a total friction value of μ_2, however we observe steadily increasing values much larger than those measured in the h_{stop} experiments.

Unless explicitly mentioned, all experimental data presented here appears dense at the free surface. Without this property, accurate measurements could not be made with our equipment. We can indirectly examine the averaged volume fraction by using the equation for global conservation of mass $q = s_1 u_s h w \phi \rho$. However, care must be taken with the unknown shape parameter s_1 in order to gain information about the volume fraction. The parameter s_1 is the product of two contributions: one from the z depth dependence and from the y transverse dependence. If the velocity profile is separable then this can be written $s_1 = s_y s_z$ where s_y is defined as

$$\int u/u_s|_{z=0}\ \mathrm{d}y, \tag{6.1}$$

which is a function of the velocity profile at the surface. We can then use this to calculate the product $s_z\phi$.

Figure 24 shows $s_z\phi$ normalised by a packing fraction of 0.58, a typical volume fraction as measured by Louge & Keast (2001). A value of 1 indicates a plug-like depth dependence, which figure 24(a) suggests is a reasonable approximation for $\theta > 36^\circ$ on the flat base. Lower inclinations have a lower value of s_z, indicating more curvature of the profile, indeed for the lowest inclinations a value of 0.6 is attained, suggesting that a Bagnold profile is also possible for a flat base.

The bumpy base exhibits a larger range of s_z as can be seen in figure 24(b). At the very lowest inclinations the value of s_z is small and suggests the presence of a static region at the base of the flow, similar to those seen in Taberlet *et al.* (2003). These are only seen for inclinations below the maximum friction angle, θ_2. For inclinations $> 36^\circ$ and $I_b < 1$, $s_z\phi$ remains very close to a value of 0.6, suggesting a Bagnold profile. In this region, there is a slight decrease with I as seen before by Forterre & Pouliquen (2008) and Baran *et al.* (2006), due to the packing fraction decaying as I increases. For higher values of I_b the flow becomes slightly more dilute at the top surface and a slip velocity develops at the base. It must be noted that for smaller values of I_b the flows have a very well defined surface, with exceedingly few saltating particles. A combination of these two factors gives rise to the large variations in $s_z\phi$, with its value ranging from more than 0.6 to less than 0.2.

Despite the flow remaining dense in the accelerating regime, the grains are not acting in the frictional manner as described by the $\mu(I)$ rheology. To first order, the grains are acting as a pseudo-viscous fluid: the resistance of the fluid is roughly proportional to Fr (see figure 12(a)), rather than being bounded above by μ_2.

There are a number of possibilities that could account for the extra resistance required to reconcile the rheology with the experimental data. One of them is that the pressure is strongly non-isotropic. If the lateral pressure is much greater than that in the z direction, the frictional force at the wall will be much larger. Another possibility is the effect of air drag on the particles at the surface. The drag force on a spherical particle is given by a Stokes' drag modified by a turbulent drag factor (see Börzsönyi & Ecke 2006)

$$F_{\mathrm{drag}} = 3\pi\mu_{\mathrm{air}} dv c(v), \tag{6.2}$$

where μ_{air} is the dynamic viscosity of air and $c(v)$ is given by $c(v) = 1{+}0.15(vd\rho_{\mathrm{air}}/\mu_{\mathrm{air}})^{2/3}$. Taking this expression and forming the ratio to the gravitational force gives the relative magnitude of the drag effect

$$\frac{F_{\mathrm{drag}}}{mg} = \frac{18\mu_{\mathrm{air}} v c(v)}{d^2\rho}. \tag{6.3}$$

The velocity at which the drag is equal to the gravitational forcing is around $7.5\,\mathrm{m\,s^{-1}}$ but only affects those particles saltating away from the bulk above the free surface. Figure 25 shows the size of this ratio as the velocity varies. As the free surface is not vertical, after the particles are ejected they rejoin the flow shortly afterwards, and so this prediction of the terminal velocity is an upper bound and will not be reached. This effect is also reduced by the flowing grains shearing the air immediately above. This means that the ambient fluid is not at rest, the relative velocities are lower and the drag is reduced. Another air-induced effect is the stress exerted by the stationary air on the free surface of the flow. However, a Prandtl boundary layer analysis reveals that this effect is small, and is around 0.1% of the gravitational forcing (see Börzsönyi & Ecke 2006, for more details).

One of the short-comings of the h_{stop} quantification of friction is that μ_1 and μ_2,

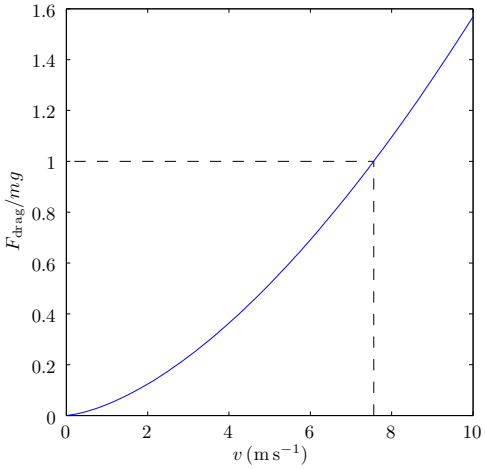

FIGURE 25. The relative effect of gravity and the turbulent air drag on a spherical particle falling vertically in an ambient fluid.

parameters relevant to the internal flow, are dependent on the boundary condition. As such, for high velocity flows, if the character of the boundary interaction changes, μ_1 and μ_2, which are defined for stopping flows, may be no longer relevant.

The pseudo-viscous effect for large I suggests that including higher order terms as an extension to the $\mu(I)$ rheology might be a good approximation. These would not effect the rheology in the regime were it has been well validated but might improved the accuracy for higher I. Such a form is

$$\mu(I) = \frac{\mu_1 I_0 + \mu_2 I + cI^2 \left(\frac{d}{h}\right)^{\alpha}}{I_0 + I} \tag{6.4}$$

where the new constants c and α are used as fit parameters. This form captures the general linear behaviour of μ for large I but is unable to capture the second-order dependence on either q or θ. The result of the fit can be seen in figure 26(a).

Plotting μ as a function of either Fr or I_b leaves unresolved dependencies on both q and θ. There are three non-dimensional groups in the problem, namely Fr, n, and θ which can be used to find a scaling law. Defining a combination of the first two as

$$I_\alpha = \frac{\mathrm{Fr}}{n^\alpha} \tag{6.5}$$

gives a modified version of I_b which collapses the data over q for each inclination for a choice of $\alpha = 1/3$ for accelerating flows. The fit is shown in figure 26(b) which suggests a linear dependence between $\mu/\tan\theta$ and $I_{1/3}$

$$\frac{\mu}{\tan\theta} = a(\theta) I_{1/3} + b(\theta) \tag{6.6}$$

for some choices of $a(\theta)$ and $b(\theta)$. The data suggest that a and b share an asymptote as well as the position at which their gradient tends to zero and as such, the functional form of the h_{stop} curve in equation (3.1) is well suited to this. We can write

$$a(\theta) = B\left(\frac{\tan(\phi_2) - \tan\theta}{\tan\theta - \tan(\phi_1)}\right) \tag{6.7}$$

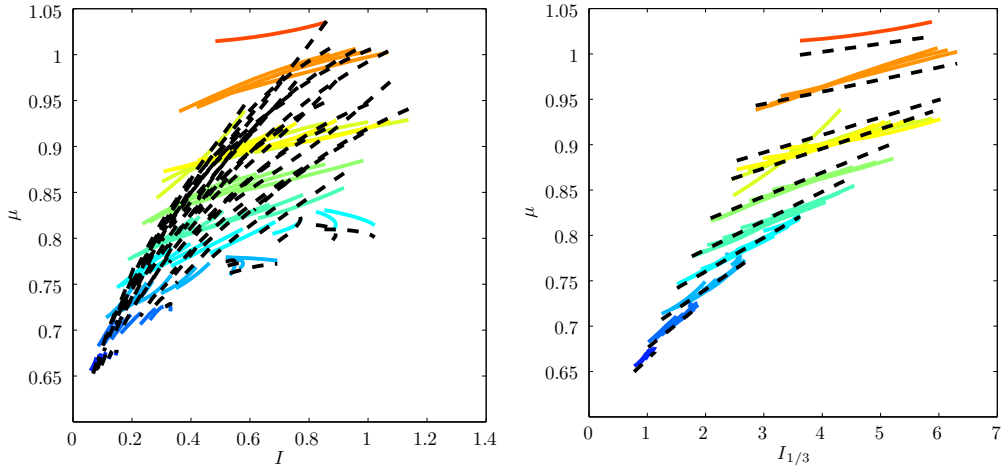

FIGURE 26. (a) Fit with I^2 extension to the $\mu(I)$ rheology. Solid lines are the experimental data, black, dashed lines are the fit curves. The fitting parameters were $\mu_1 = 0.58$, $\mu_2 = 0.82$, $I_0 = 0.37$, $c = 0.0015$, $\alpha = -2$. (b) μ plotted against $I_{1/3}$ (time-steady flows removed). Black, dashed lines give fit of data using the θ dependence in equation (6.8).

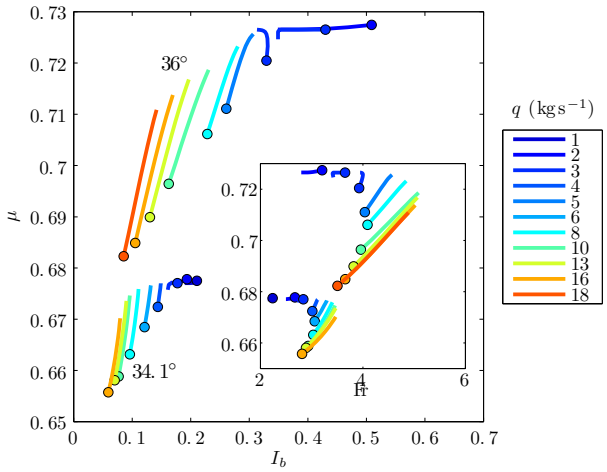

FIGURE 27. Behaviour of effective friction at low inclinations as a function of I_b and Fr. Dot indicates measurement at top of chute.

where upon fitting, $B = 0.03$, $\phi_1 = 23.1°$ and $\phi_2 = 55.9°$. This gives the representation

$$\frac{\mu}{\tan\theta} = a(\theta)\left[1.5 + I_{1/3}\right] + 0.75. \tag{6.8}$$

This relationship removes the friction angles deduced from h_{stop} experiments from the rheology and replaces them with two other generalised friction angles. The larger angle corresponds to the point after which $\mu/\tan\theta$ is constant, and is coincidentally the highest inclination for which experiments were carried out. At these high inclinations, μ saturates at around $0.8\tan\theta$.

In order to reconcile this analysis with previous studies, it is necessary to investigate the angles for which equilibrium states exist in more detail. We plot μ as a function

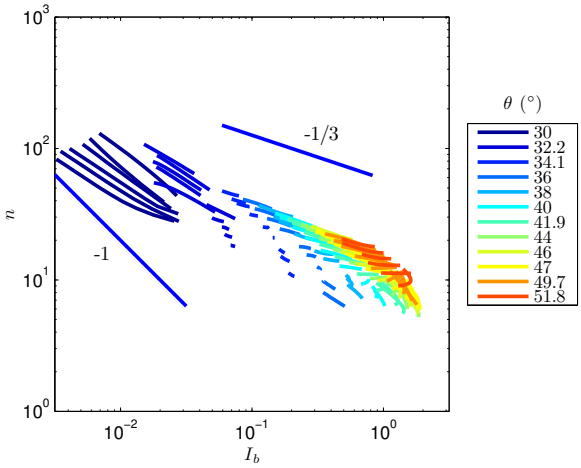

FIGURE 28. Log plot of n against I_b for the bumpy base.

of I_b for two inclinations in figure 27 and against Fr in the inset. The first inclination, $\theta = 34.1°$ is just below the angle of vanishing h_{stop} $\theta_2 = 34.2°$, and the second one above at $\theta = 36°$. At the lowest mass fluxes, both inclinations indeed exhibit flows with constant friction coefficient. For the lower inclination, these flows are not accelerating as constant Fr (or equivalently I_b) is achieved down the slope. At the higher inclination, Fr and I_b decrease as the flow progresses. The start point for each flow is marked with a dot. The values of μ for these flows are in agreement with the values recorded in the h_{stop} experiments, and therefore also agree with the numerically-investigated rheology. A slight complication is introduced as μ is no longer a single valued function of either Fr or I_b possibly due to the stabilising influence of the sidewalls. The change in μ at $\theta = 36°$ as q varies is around 7%, and drops to 4% for 34.1°. It is also interesting to note that accelerating flows for these low inclinations are collapsed over q when using $I_{1/3}$ as the appropriate non-dimensional number, whereas the flows with constant μ are not. Steady μ flows are well explained by the $\mu(I)$ rheology, whereas the accelerating flows need an extra rheological contribution to explain the behaviour. It is proposed that $I_{1/3}$ gives the appropriate scaling for these extra contributions.

A further indication of a difference in regime can be seen in figure 28, which shows a log-log plot of the dependence of h/d on I_b. Manipulation of the $\mu(I)$ equations (1.1) and (3.1) gives

$$I_b = -\gamma n^{-1} + \beta \left(\frac{\tan\theta - \mu_1}{\mu_2 - \tan\theta} \right). \tag{6.9}$$

The low inclinations for which this rheology is expected to work does exhibit a slope of gradient -1, but quickly changes as the inclination increases. The accelerating flows exhibit a behaviour such that $I_b \sim n^{-3}$. Given that μ is no longer simply a function of a parameter such as I_b, and different scalings are required to collapse the accelerating and constant μ regimes, it is possible that other flow variables such as granular temperature are needed to fully describe the system.

The form proposed in equation (6.8) predicts that the flow cannot reach a steady velocity above $\theta = \phi_2$. Below this threshold, the terminal state is given by $I_{1/3} = 0.25/a(\theta) - 1.5$. Above this threshold, the total friction μ is always less than the maximum value $\mu = 0.75 \tan\theta$, resulting in an constantly accelerating flow.

However, DEM simulations for flows on high angles suggest that non-accelerating states

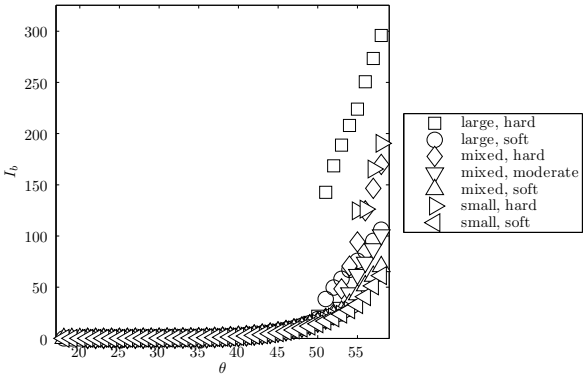

FIGURE 29. Terminal state of flow simulations using different particle species. The time-steady state value of I_b is plotted for various q and θ.

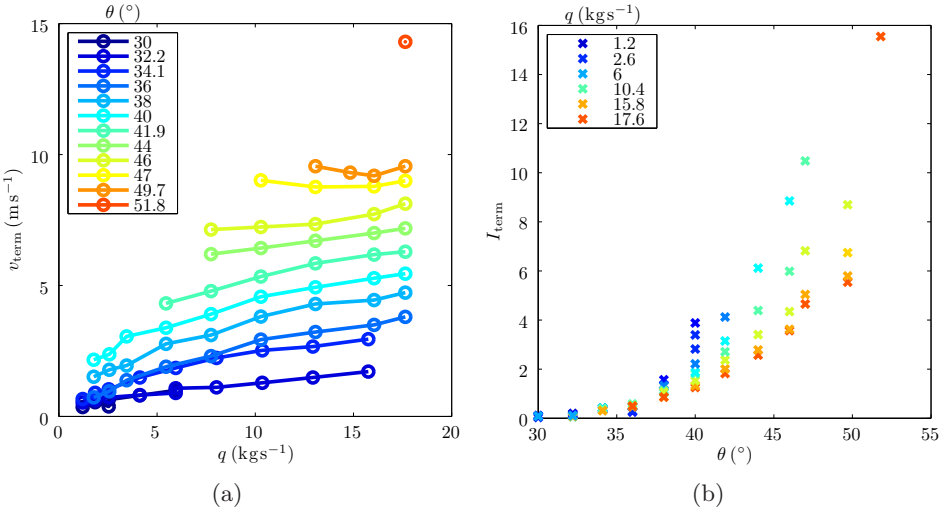

FIGURE 30. (a) The terminal velocity of full-width flows on a bumpy base as predicted by the fit formula (3.4). Each line represents the terminal velocities at a given inclination as the flux varies. (b) The terminal value of I, I_{term} as it varies with q and θ. The value of h used in the calculation is calculated from q, assuming a constant ϕ.

can exist, although they are not dense throughout their depth. Figure 29 shows the steady state value of I_b for multiple θ, q, and particle species. At these high values of I_b, the particle stiffness and size become important as the dissipation during inelastic collisions provides another mechanism for energy dissipation. For lower inclinations, the variation in terminal I_b is very small between different particle species. For the high inclination flows, the final state is periodic, where the flow separates from the base and shortly after falls, colliding with the base again dissipating energy, allowing $\mu \to \tan\theta$, at least in an averaged sense. In order to replicate this in the lab, the chute would need to be many kilometres long. It is also not clear if the ambient fluid would have a significant effect on the flow in this state.

The fitting function in equation (3.4) also can be manipulated to give a prediction of if a terminal velocity v_{term}exists. If $\kappa > 0$ then v_{term} can be calculated by $v_{\text{term}}^2 = u_0^2 + \beta/\kappa$. For flows with a constant velocity in the chute, v_{term} is taken directly from the data.

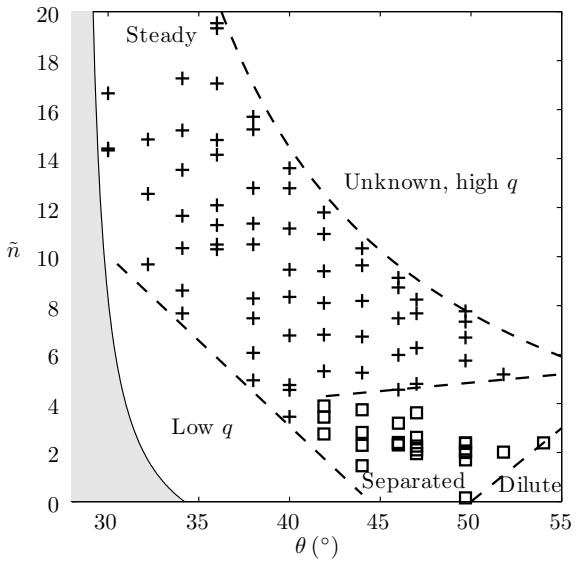

FIGURE 31. Phase diagram showing how the predicted terminal mass hold up $\tilde{n}$ and θ vary. (+) indicates flows with a predicted constant velocity terminal state and (□) indicates flows that have a predicted steady state, but have separated at the wall. No data exists for the dilute flows as n is ill defined there. There is also no data for low flow rates q as the apparatus was sensitive to cross slope variation in the initial condition for very thin flows. The shaded area shows where $h < h_{\text{stop}}$ and heap flow occurs.

Although care must be taken when extrapolating data outside of the observed range, all but one of the terminal velocities were less than double the velocity at the end of the chute. This indicates it is not unreasonable to expect that the flow, when at the extrapolated velocity, is in a dense state similar to how it is observed in the chute, and so the extrapolated terminal state is a likely outcome. If the flow undergoes a phase transition then the development is likely to be substantially different to the extrapolated development.

Figure 30 shows the terminal velocity v_{term}, and terminal inertial number I_{term} (when they exist) for flows over the bumpy base. Figure 30(a) shows v_{term} as a function of the control parameters θ and q. A clear structure is shown where the terminal velocity is a strong function of the inclination, especially at high inclinations. Indeed, for flows over 51.8° no steady flows were predicted by the extrapolation, perhaps indicating that there is still an upper limit to the friction, albeit much higher than the values measured from h_{stop} experiments. The dependence of v_{term} on the mass flux, q, is also increasing. However, as q increases, the dependence weakens suggesting that the terminal velocity will become independent of the mass flux (and therefore the flow height). This is possibly due to the wall friction giving an increased contribution as the flow deepens.

The second subfigure 30(b) shows the terminal value of the inertial parameter I_{term}, as a function of θ. If I is indeed the only parameter that governs the flow then we would expect total collapse of the data in this graph, however there is still significant spread. Plotting the data in terms of $I_{1/3}$ as in figure 26(b) does not significantly improve the collapse of the data either.

The predicted values of the steady state mass hold-up $\tilde{n} = n\phi/0.58$ can be seen in figure 31. In contrast to the $\mu(I)$ rheology which predicts that for flows on inclinations $\theta > \theta_2$ should have an indefinite, linear acceleration, we see that steady states are possible

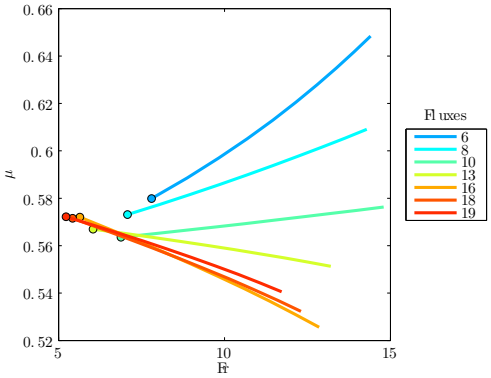

FIGURE 32. μ on a flat base, inclination 40° for varying fluxes. Dots indicates measurement at top of chute

in this region. Also shown is the shaded region underneath the h_{stop} curve, in which a heap will form with a flowing layer on top of it. At the other end of the space, for high inclinations and small $\tilde{n}$ we see the predicted steady state for the separated flows. As no data was available for the dilute flows (as n is ill-defined), the boundaries of this area of the phase plane were estimated.

There are no data for very low fluxes $q < 1\,\mathrm{kg\,s^{-1}}$ as the apparatus tended to produce a low energy, uneven saltating state, which is initiated by the drop from the hopper to the chute, again making n ill-defined.

The flows over a flat base did not exhibit such a rich range of behaviours. The data set was much smaller as transverse separation affected a large proportion of the flows, and has therefore been excluded from most of the analysis. Figure 12(b) shows that μ is invariably lower than on the bumpy base, as the flat base gives less resistance. The range of μ seen over the small base is much lower, and is almost uniform for all Fr. This fits in well with the h_{stop} data, which only gave a difference of 0.2° between θ_1 and θ_2. As a result, the $\mu(I)$ model with constant μ_i gives good agreement with the data. It it not clear if the flows on the flat base will approach a terminal velocity in the same way as the bumpy base. Since the acceleration of these flows is approximately linear, the fit (3.4) is degenerate for three parameters, meaning that κ, and therefore the extrapolated terminal velocity is very sensitive to small amounts of noise.

However, this zeroth order, sliding block model cannot capture the cross-slope velocity variation. As the flow accelerates, mass conservation dictates that if ϕ stays constant, then the height must decrease and the flow must elongate. This elongation will then excite an internal flow structure, generating transverse gradients in the stress and ultimately the cross-slope velocity profile seen at the surface.

Figure 32 shows an interesting dependence of μ on the mass flux for the flat base. Low mass fluxes demonstrate the expected behaviour of μ increasing with Fr. However, as the mass flux increases, the gradient of this slope decreases until it becomes negative. This effect is seen for all of the fully dense flows investigated here. Having a negative gradient of $\mu(\mathrm{Fr})$, indicates that in this regime the flows will accelerate faster and faster until a flow transition occurs or other forces come into effect.

7. Conclusion

Previous work on granular flows has concentrated on $I < 0.5$ (MiDi 2004). The $\mu(I)$ rheology and the flow rule $\mathrm{Fr} = -\gamma + \beta\frac{h}{h_{\mathrm{stop}}}$ have been successful in predicting the dynamics of such flows. However, they suggest that no non-accelerating flows are possible for $\theta > \tan^{-1}\mu_2$ since $h_{\mathrm{stop}} = 0$. Our experiments show that these models are inaccurate for larger θ and that steady flows could be possible on much steeper slopes. A number of interesting instabilities were also observed. We have observed a transverse separation where a dense core in the middle of the chute is flanked by dilute regions which grow in size down the chute. We have also seen a transition where the entire bulk of the flow becomes energised, unstable and dilute. A transverse velocity profile instability in the form of longitudinal vortices was also seen for intermediate inclinations.

Flows over the flat base are well-modelled by constant total friction. Although there was some complicated variation with the Froude number and flow depth, it was small compared to the range of the total friction on the bumpy base. However, a significant cross slope velocity variation was observed that is incompatible with some granular models which predict a plug flow over flat surfaces. Development of a model to capture these effects remains a subject for future work. Of particular interest would be the comparison of this data with the 3d numerical simulations of kinetic theory.

The authors would like to thank Michele Louge, Barbara Turnbull and Stuart Dalziel for many useful ideas for the design and operation of the chute. Particular thanks are due to David Page-Croft and all the DAMTP technical staff who have spent years building and maintaining the equipment. The chute was funded by EPSRC grant GR/T02416/01, JNM was supported by an EPSRC ARF and AJH was supported by an NERC studentship.

REFERENCES

Ahn, H., Brennen, C.E. & Sabersky, R.H. 1991 Measurements of velocity, velocity fluctuation, density, and stresses in chute flows of granular materials. *Journal of Applied Mechanics* **58** (792), 12.

Ahn, H., Brennen, C.E. & Sabersky, R.H. 1992 Analysis of the fully developed chute flow of granular materials. *Journal of Applied Mechanics* **59**, 109.

Ancey, C., Coussot, P. & Evesque, P. 1999 A theoretical framework for granular suspensions in a steady simple shear flow. *Journal of Rheology* **43**, 1673.

Baran, O., Ertaş, D., Halsey, T.C., Grest, G.S. & Lechman, J.B. 2006 Velocity correlations in dense gravity-driven granular chute flow. *Physical Review E* **74** (5), 051302.

Börzsönyi, T. & Ecke, R.E. 2006 Rapid granular flows on a rough incline: Phase diagram, gas transition, and effects of air drag. *Physical Review E* **74** (6), 061301.

Börzsönyi, T., Ecke, R.E. & McElwaine, J.N. 2009 Patterns in Flowing Sand: Understanding the Physics of Granular Flow. *Physical review letters* **103** (17), 178302.

Delannay, R., Louge, M., Richard, P., Taberlet, N. & Valance, A. 2007 Towards a theoretical picture of dense granular flows down inclines. *Nature Materials* **6** (2), 99–108.

Ertaş, D., Grest, G.S., Halsey, T.C., Levine, D. & Silbert, L.E. 2001 Gravity-driven dense granular flows. *EPL (Europhysics Letters)* **56**, 214.

Forterre, Y. 2006 Kapiza waves as a test for three-dimensional granular flow rheology. *Journal of Fluid Mechanics* **563**, 123–132.

Forterre, Y. & Pouliquen, O. 2001 Longitudinal vortices in granular flows. *Physical Review Letters* **86** (26), 5886–5889.

Forterre, Y. & Pouliquen, O. 2003 Long-surface-wave instability in dense granular flows. *Journal of Fluid Mechanics* **486**, 21–50.

Forterre, Y. & Pouliquen, O. 2008 Flows of dense granular media. *Annual Review of Fluid Mechanics* **40** (1), 1–24.

Goldhirsch, I. 2003 Rapid granular flows. *Annual review of fluid mechanics* **35**, 267–293.

Gray, J., Wieland, M. & Hutter, K. 1999 Gravity-driven free surface flow of granular avalanches over complex basal topography. *Proceedings of the Royal Society of London. Series A: Mathematical, Physical and Engineering Sciences* **455** (1985), 1841.

Jackson, R. 1983 Theory of dispersed multiphase flow.

Janssen, HA 1895 Tests on grain pressure silos. *Zeits. d. Vereins Deutsch Ing* **39** (35), 1045–9.

Jenkins, James & Berzi, Diego 2010 Dense inclined flows of inelastic spheres: tests of an extension of kinetic theory. *Granular Matter* **12**, 151–158, 10.1007/s10035-010-0169-8.

Jenkins, JT & Richman, MW 1985 Kinetic theory for plane flows of a dense gas of identical, rough, inelastic, circular disks. *Physics of Fluids* **28**, 3485.

Jop, P., Forterre, Y. & Pouliquen, O. 2005 Crucial role of sidewalls in granular surface flows: consequences for the rheology. *Journal of Fluid Mechanics* **541**, 167–192.

Jop, Pierre, Forterre, Yoel & Pouliquen, Olivier 2006 A constitutive law for dense granular flows. *Nature* **441**.

Louge, M.Y. & Keast, S.C. 2001 On dense granular flows down flat frictional inclines. *Physics of Fluids* **13**, 1213.

McNamara, S. & Young, WR 1994 Inelastic collapse in two dimensions. *Physical Review E* **50**, 28–31.

MiDi, GDR 2004 On dense granular flows. *The European Physical Journal E: Soft Matter and Biological Physics* **14** (4), 341–365.

Mitarai, Namiko & Nakanishi, Hiizu 2005 Bagnold scaling, density plateau, and kinetic theory analysis of dense granular flow. *Phys. Rev. Lett.* **94**, 128001.

Nedderman, RM, Tuzun, U., Savage, SB & Houlsby, GT 1982 The flow of granular materials–i:: Discharge rates from hoppers. *Chemical Engineering Science* **37** (11), 1597–1609.

Patton, JS, Brennen, CE & Sabersky, RH 1987 Shear flows of rapidly flowing granular materials. *Journal of Applied Mechanics* **54**, 801.

Pouliquen, O. 1999 Scaling laws in granular flows down rough inclined planes. *Physics of fluids* **11**, 542.

Pouliquen, O., Cassar, C., Jop, P., Forterre, Y. & Nicolas, M. 2006 Flow of dense granular material: towards simple constitutive laws. *Journal of Statistical Mechanics: Theory and Experiment* **2006**, P07020.

Savage, S.B. 1979 Gravity flow of cohesionless granular materials in chutes and channels. *J. Fluid Mech* **92** (1), 53–96.

Savage, S.B. 1984 The mechanics of rapid granular flows. *Advances in applied mechanics* **24**, 289–366.

Savage, SB & Hutter, K. 1989 The motion of a finite mass of granular material down a rough incline. *Journal of Fluid Mechanics* **199** (-1), 177–215.

Silbert, L.E., Ertaş, D., Grest, G.S., Halsey, T.C., Levine, D. & Plimpton, S.J. 2001 Granular flow down an inclined plane: Bagnold scaling and rheology. *Physical Review E* **64** (5), 51302.

Sveen, J. K. & Dalziel, S. B. 2005 A dynamic masking technique for combined measurements of PIV and synthetic schlieren applied to internal gravity waves. *Measurement Science and Technology* **16**, 1954–1960.

Taberlet, N., Richard, P., Jenkins, JT & Delannay, R. 2007 Density inversion in rapid granular flows: the supported regime. *The European Physical Journal E* **22** (1), 17–24.

Taberlet, N., Richard, P., Valance, A., Losert, W., Pasini, J.M., Jenkins, J.T. & Delannay, R. 2003 Superstable granular heap in a thin channel. *Physical review letters* **91** (26), 264301.

White, DJ 2003 PSD measurement using the single particle optical sizing (SPOS) method. *Géotechnique* **53** (3), 317–326.